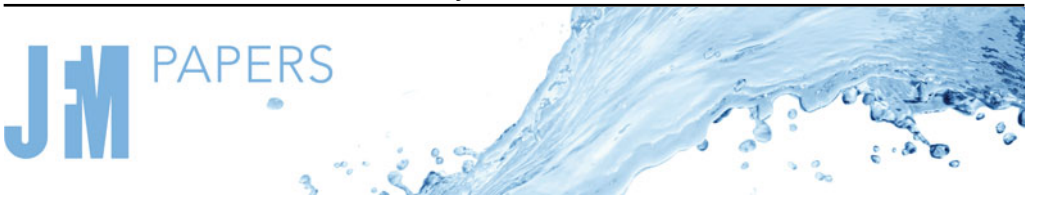
J. Fluid Mech. (2026), *vol.* 1035, A4, doi:10.1017/jfm.2026.11516



Flow inside a square cavity driven by the symmetric sliding of its four sides

Fernando Mellibovsky[1], **Bo An**[2,3], **Josep M. Bergadà**[4] and **Alvaro Meseguer**[5]

[1]Departament de Física, Division of Aerospace Engineering, Universitat Politècnica de Catalunya, 08034 Barcelona, Spain

[2]Northwestern Polytechnical University, School of Aeronautics, Xi'an 710072, PR China

[3]National Key Laboratory of Aircraft Configuration Design, Xi'an 710072, PR China

[4]Department of Fluid Mechanics, Universitat Politècnica de Catalunya, 08034 Barcelona, Spain

[5]Departament de Física, Universitat Politècnica de Catalunya, 08034 Barcelona, Spain

Corresponding authors: Fernando Mellibovsky, fernando.mellibovsky@upc.edu; Bo An, bo_alan_an@163.com

(Received 6 October 2025; revised 4 April 2026; accepted 4 April 2026)

We investigate the incompressible flow inside a two-dimensional square cavity, driven by the sliding motion of its four lids, all at the same speed and with facing lids moving in opposite directions. The problem has three symmetries: two mirror symmetries with respect to the diagonals and a π rotation invariance about the centre of the cavity. The base flow, a steady state that has all three symmetries, is the unique solution at sufficiently low values of the Reynolds number (Re) and acts as a global attractor. At higher Re, it has become unstable and shares the phase space with a globally attracting space–time symmetric periodic orbit that, in addition to the rotational invariance, is also invariant under evolution over half a period followed by reflection about either of the diagonals. In between, a wealth of solution branches and intervening bifurcations mediate the transition process. In particular, a pair of steady states that break the mirror symmetries but are mirror-symmetry images of each other regulate the appearance and disappearance of a second space–time symmetric periodic orbit and a pair of asymmetric periodic orbits that are also mirror images of each other. The catalogue of instabilities includes both local (two pitchfork, two Hopf, a saddle-node and a cyclic fold) and global (two heteroclinic and one homoclinic) bifurcations. The sequence of transitions is explained in terms of a one-dimensional path through the parameter space of a codimension-four bifurcation: the double zero bifurcation with Z_2 symmetry and degeneracy of the third order terms.

Key words: instability, nonlinear dynamical systems, bifurcation

© The Author(s), 2026. Published by Cambridge University Press. This is an Open Access article, distributed under the terms of the Creative Commons Attribution licence (https://creativecommons.org/licenses/by/4.0/), which permits unrestricted re-use, distribution and reproduction, provided the original article is properly cited.

https://doi.org/10.1017/jfm.2026.11516 Published online by Cambridge University Press

1. Introduction

The incompressible flow inside a square cavity, driven by the tangential motion of one of its sides, has long served as a model problem in fluid mechanics (Shankar & Deshpande 2000; Kuhlmann & Romanò 2019) for the study of wall-bounded vortex dynamics, centrifugal and shear flow instabilities, or laminar–turbulent transition within enclosed containers, to name but a few complex flow phenomena of interest. Because of its compelling simplicity, the so-called lid-driven square cavity (LDSC) flow problem, has readily become a classic benchmark for the validation of numerical codes that solve the Navier–Stokes equations (Ghia, Ghia & Shin 1982; Schreiber & Keller 1983; Vanka 1986; Gresho & Chan 1990; Hou *et al.* 1995; Botella & Peyret 1998; Auteri *et al.* 2002*b*; Sahin & Owens 2003*a*; Gupta & Kalita 2005; Bruneau & Saad 2006; Marchi, Suero & Araki 2009; Khorasanizade & Sousa 2014; Romanò & Kuhlmann 2017).

Although the first instability of the LDSC base flow in an infinite-span domain is three-dimensional (3-D) in nature (Koseff & Street 1984; Aidun, Triantafillopoulos & Benson 1991; Benson & Aidun 1992; Albensoeder, Kuhlmann & Rath 2001; Theofilis, Duck & Owen 2004; Non, Pierre & Gervais 2006), which corresponds to a disruption of the translational spanwise invariance that results in an infinite array of steady Taylor–Görtler vortices of wavenumber $\kappa_{3D} \simeq 15.4\, L^{-1}$ beyond $Re_{3D} = LU/\nu \simeq 785$, the purely two-dimensional (2-D) bifurcation scenario constitutes a much more convenient set-up for benchmarking hydrodynamic stability codes. Here, L is the streamwise size of the lid, U its sliding velocity and ν the kinematic viscosity of the fluid.

Regularisation of the sliding lid boundary condition to avoid the singularity at the corners has the 2-D LDSC first destabilise in a supercritical Hopf bifurcation at $Re_H = 10\,267 \pm 12$ with non-dimensional angular frequency $\omega_H \simeq 2.080\, L/U$ (Shen 1991; Fortin *et al.* 1997; Abouhamza & Pierre 2003). The type and nature of the bifurcation remains the same for LDSC with corner singularities, but the instability is promoted to $Re_H \simeq 8020$ and the angular frequency higher at $\omega_H \simeq 2.83\, L/U$ (Poliashenko & Aidun 1995; Fortin *et al.* 1997; Cazemier, Verstappen & Veldman 1998; Tiesinga, Wubs & Veldman 2002; Abouhamza & Pierre 2003; Peng, Shiau & Hwang 2003; Sahin & Owens 2003*b*; Bruneau & Saad 2006; Boppana & Gajjar 2010; Kalita & Gogoi 2016; Nuriev, Egorov & Zaitseva 2016; Murdock, Ickes & Yang 2017).

The periodic solution resulting from the Hopf bifurcation undergoes a Neimark–Sacker bifurcation at $Re_{NS} \simeq 9150$ with modulational frequency $\omega_{NS} \simeq 1.7\, L/U$ (Tiesinga *et al.* 2002), in fair agreement with the characteristic properties of quasiperiodic solutions reported in the literature at slightly higher Reynolds numbers (Poliashenko & Aidun 1995; Cazemier *et al.* 1998; Auteri *et al.* 2002*a*). An analysis of the steady state beyond the original Hopf instability reveals a sequence of further supercritical Hopf bifurcations whose properties anticipate the upcoming Neimark–Sacker bifurcation (Tiesinga *et al.* 2002). The chaotic dynamics that follows shortly after the emergence of quasi-periodicity have been shown to result from a classic Ruelle–Takens scenario (Ruelle & Takens 1971; Newhouse, Ruelle & Takens 1978).

This is a rather dull bifurcation sequence that does not provide all necessary ingredients to test hydrodynamic stability codes to their fullest. In particular, it lacks fold bifurcations, which are required to validate steady and periodic state continuation codes, or global bifurcations involving homoclinic or heteroclinic orbits. Furthermore, the first bifurcation occurs at a rather large value of the Reynolds number, which poses a further complication by requiring particularly fine space and time discretisations, and the ensuing need of intensive computational resources. Finally, the problem lacks any kind of symmetries,

https://doi.org/10.1017/jfm.2026.11516 Published online by Cambridge University Press

such that no allowance is made for the appearance of the rich bifurcation scenarios that typically arise in their presence.

All three shortcomings can be overcome by simply setting a second or all four walls of the square cavity in motion. This increases the parameter count to two and four, respectively, and, by setting all lid velocities to the same value or to two different values in pairs, symmetries might be introduced that greatly enrich the dynamics of the problem. In the case of all four walls moving at the same velocity, with facing walls sliding in opposite directions, transitional dynamics are brought to much lower Re and become particularly complex. The model is, from a mathematical standpoint, as simple as the classic LDSC flow problem, but provides a much broader benchmark for testing numerical schemes intended for the continuation of solution branches and the analysis of all sorts of bifurcations, both local and global, in the presence or absence of symmetries.

The 4-lid-driven symmetric square cavity (4LDSSC) flow undergoes a symmetry-breaking steady bifurcation at $Re_{P_1} \simeq 129$ that results in two branches of mutually symmetric solutions (Wahba 2009; Perumal & Dass 2011). The mirror symmetry about both diagonals is broken, but an invariance to rotations of angle π about the cavity centre persists. While the already unstable branch of symmetric solutions undergoes a second pitchfork bifurcation at $Re_{P_2} \simeq 359$ (Cadou, Guevel & Girault 2012; Zhuo *et al.* 2013), both a Hopf (Wahba 2011; Zhuo *et al.* 2013, 2015) and a steady bifurcation (Cadou *et al.* 2012), for which the symmetry-breaking or preserving nature was not specified, have been inconsistently reported for the branch of asymmetric solutions at values of the Reynolds number of $Re \simeq 720$ and $Re \simeq 867$, respectively. A long period limit cycle has been observed to attract the dynamics beyond the alleged Hopf bifurcation, whose super (Wahba 2011) or subcriticality (Zhuo *et al.* 2013, 2015) has not been established. The periodic state, which preserves the π-rotational invariance, evolves in the vicinity of one of the asymmetric steady states for half a period and of its symmetry-conjugate counterpart for the other half, periodically switching from one to the other.

A leap forward in clarifying the bifurcation diagram of the 4LDSSC flow was undertaken by Chen *et al.* (2013) employing pseudo-arclength continuation and Arnoldi stability analysis of steady states. The first and second pitchfork bifurcations were confirmed at $Re_{P_1} = 130.29$ and $Re_{P_2} = 355.45$, and the two corresponding branches of asymmetric states found to coalesce in a saddle-node bifurcation at $Re_{SN} = 877$, which might possibly be the secondary steady bifurcation reported by Cadou *et al.* (2012). The symmetric steady state, which becomes unstable at the first pitchfork as a pair of stable conjugate-symmetric asymmetric state branches is issued, was found to remain unstable beyond the second pitchfork. At this point, a second pair of unstable asymmetric state branches is created. In contrast to expectation, the stable pair of asymmetric solutions was not seen to undergo a secondary Hopf bifurcation and reached instead the saddle-node bifurcation with their stability intact.

Regardless of the occurrence or otherwise of a Hopf bifurcation, no stable steady state remains beyond the saddle-node bifurcation. The aforementioned periodic orbit is left as the only stable solution for a moderate Re range before eventually triggering the onset of chaotic dynamics. It is one of the main aims of this paper to elucidate the origin of this periodic solution, seemingly disconnected from the base symmetric state, in terms of global bifurcations involving the various known solutions, and to clarify how the two disjoint symmetrical regions of phase space, each with its own symmetry-related objects, become dynamically connected. In this respect, the 2-D 4LDSSC problem serves as one of the simplest flow set-ups to illustrate a mechanism whereby statistical symmetry is eventually recovered after a temporary loss. This mechanism may be at play in more complex, experimentally realisable, 3-D flows belonging to the class of problems in fluid

https://doi.org/10.1017/jfm.2026.11516 Published online by Cambridge University Press

mechanics that feature mirror symmetries. Specifically, those that undergo an intermediate regime of stable symmetry-breaking solution branches between the symmetric base state that acts as the global attractor at low Re and the statistically symmetric turbulent (or chaotic) state observed at high Re. See, for example, the spiral and turbulent spiral regimes in the Taylor–Couette system, separating the stability regions of the circular Couette flow and featureless turbulence (Coles 1965; Andereck, Liu & Swinney 1986; Meseguer *et al.* 2009; Wang *et al.* 2023).

3-D 4LDSSC bounded in the spanwise direction by stationary walls has been shown to preserve, for low aspect ratios, the problem symmetry to higher Re as compared with 2-D simulations (Li & Maa 2017). The stabilising effect of the walls is reduced as the aspect ratio is increased and the critical Re_{P_1} for the symmetry breaking bifurcation diminishes, but remains high at 319 for an aspect ratio of 3. The flow patterns at midspan are, however, topologically close to those of the 2-D cavity in both the pre- and post-critical regimes. It is nevertheless unclear whether the infinite-span case will remain 2-D across much of the bifurcation scenario reported in the literature. Be it as it might, the low-Re flow dynamics in 2-D cavities is relevant to the understanding of the onset of 2-D turbulence (Molenaar, Clercx & van Heijst 2005), an active research field on account of its sharing key features with the large-scale motions observed in geophysical flows (Boffetta & Ecke 2012). Wall-bounded 2-D vortices do indeed occur in near-shore zones, such as at the head of rip currents (Smith & Largier 1995) or in tidal channels (Wells & van Heijst 2003). In particular, the flow set-up we have adopted serves as a simple model for the onset of chaos, a necessary step towards 2-D turbulence, when the base flow consists of two strong opposing jets (issued in our case from the two corners where the lids run into each other) that meet at the centre of a narrowly confined domain. Furthermore, the relevance of analysing bifurcation sequences of unstable solutions in symmetry-restricted domains reaches much further than its mere use for code validation or as a model for the onset of 2-D turbulence. The strange saddle that is embedded in chaotic motion, and therefore organises turbulent dynamics, consists of collections of unstable solutions and their connecting manifolds (Procaccia 1988). Restricting the analysis to certain symmetries or severely truncated domains, however unrealistic this may appear from a merely experimental point of view, allows for a detailed analysis that is otherwise unattainable and provides access to the basic ingredients that might be at play in the real problem (Hof *et al.* 2004; de Lozar *et al.* 2012; Ritter, Mellibovsky & Avila 2016). In the case of systems that feature translational invariance along an extended spatial coordinate, one such possible symmetry-restriction consists in constraining the dynamics to be 2-D (Jimenez 1990; Mellibovsky & Meseguer 2015).

A notorious complication of simulating the flow inside lid-driven cavities is the infamous singularity at the corners where the sliding lid meets the adjoining stationary walls. Although some studies have devised strategies to soundly address the singularity (Gupta, Manohar & Noble 1981; Botella & Peyret 2001; Auteri *et al.* 2002*b*), low-order space discretisations have the advantage of confining its effects to the immediate vicinity of the corners, such that the issue is more often than not disregarded as irrelevant on account of its being of little consequence to the global flow dynamics. High-order discretisations, such as those typically resulting from the use of spectral methods, are however extremely sensitive to the singularity and cannot overlook its decided impact on the bulk flow. A standard fourth-order polynomic regularisation has occasionally been applied to the lid velocity distribution to avoid the singularity (Shen 1991; Botella 1997) but, although the flow allegedly preserves the qualitative dynamics of the original singular cavity, the quantitative effects are non-negligible. A rather simple means of simulating

https://doi.org/10.1017/jfm.2026.11516 Published online by Cambridge University Press

quasi-singular cavity flows and reduce the quantitative impact to a minimum resorts to the enforcement of a high-order regularisation that achieves a constant velocity over a wider extent of the lid while still removing the singularities at the corners (Batoul, Khallouf & Labrosse 1994). Meseguer *et al.* (2024) tackled the 4LDSSC problem with a spectral discretisation and high-order regularisation to unfold the full diagram as regards to steady states and their local bifurcations. In addition to generally confirming the scenario presented by Chen *et al.* (2013) for the non-regularised case, their detailed analysis further produced hitherto unknown bifurcations and steady solution branches that, unlike all previously known bifurcations and states, also break the π rotational symmetry.

Back to the π rotationally invariant scenario, and piecing together the states and bifurcations reported in the literature for the 4LDSSC, there seems to be strong evidence advocating for the hypothesis that a degenerate double-zero bifurcation with Z_2 symmetry might be in place. The normal form for this codimension-four bifurcation was first derived by Knobloch (1986) and then unfolded by Dangelmayr, Neveling & Armbruster (1986), following earlier work on a partial unfolding of a closely related codimension-three bifurcation by Dangelmayr, Armbruster & Neveling (1985). The associated phase portraits have all the ingredients to explain the observations of the 4LDSSC problem in terms of a one-dimensional (1-D) path across the four-dimensional parameter space in the vicinity of the codimension-four point. In this work, we address the fluid flow problem from a dynamical systems perspective and explore the possible occurrence of a degenerate symmetric double zero bifurcation. Specifically, we are interested in the origin of the long-period space–time-symmetric periodic orbit that is responsible for the onset of chaos at higher Re. In addition to this orbit, all steady solution branches and connecting steady bifurcations discussed here were already known. In this paper, we contribute the missing pieces: two Hopf bifurcations, the two resulting short-period cycles (one space–time symmetric and an asymmetric but mutually symmetric pair) and, foremost, three global bifurcations (two heteroclinic and one homoclinic bifurcation), each involving one of the periodic orbits and the same pair of saddle asymmetric steady states.

The paper is structured as follows. The 4LDSSC flow problem is formulated in § 2 along with a brief outline of the methods employed in its analysis. Section 3 presents an overview of the bifurcation diagram. The full catalogue of solutions is exhibited and every state duly characterised in § 4 (and Appendix A), followed by a brief description of all observed phase map topologies in § 5. Section 6 undertakes the minute dissection of all local and global bifurcations, which are then explained in the context of a codimension-four bifurcation in § 7. Finally, concluding remarks are presented and prospective lines of research explored in § 8.

2. Methods

Consider the incompressible flow within a 2-D square enclosure driven by the tangential motion of its four bounding sides at constant and equal velocity, with facing walls sliding in opposite directions (see figure 1). The flow dynamics is governed by the incompressible Navier–Stokes equations, which, after suitable non-dimensionalisation with lid size L and velocity U as length and velocity scales, result in

$$\partial_t \boldsymbol{u} + (\boldsymbol{u}\cdot\boldsymbol{\nabla})\boldsymbol{u} = -\boldsymbol{\nabla} p + \frac{1}{Re}\Delta\boldsymbol{u},$$
$$\boldsymbol{\nabla}\cdot\boldsymbol{u} = 0, \tag{2.1}$$

where $\boldsymbol{u} = \boldsymbol{u}(\boldsymbol{x}; t) = (u, v)$ and $p = p(\boldsymbol{x}; t)$ are the velocity and pressure fields, and t and $\boldsymbol{x} = (x, y) \in [-0.5, 0.5] \times [-0.5, 0.5]$ the time and space coordinates. The sole governing

https://doi.org/10.1017/jfm.2026.11516 Published online by Cambridge University Press

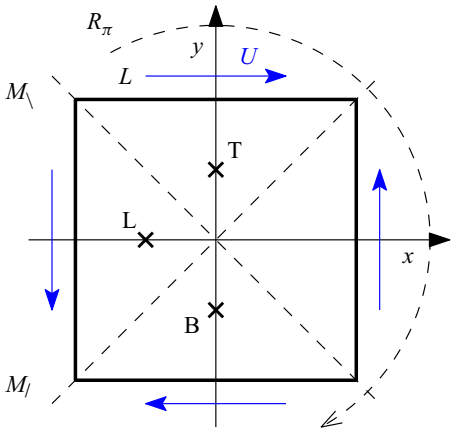


Figure 1. Sketch of the 4LDSSC of side L and lid velocity U. The mirror symmetry lines ($M_\backslash$ and $M_/$) and the π-rotation invariance (R_π) of the problem are indicated with dashed lines. Points T, L and B, half-way between the origin and the top, left and bottom walls, respectively, indicate the probe locations used in the analysis of solutions.

parameter is the Reynolds number $Re = UL/\nu$, with ν the kinematic viscosity of the fluid. No-slip boundary conditions are enforced on all four walls by setting a constant tangential unit velocity.

$$\boldsymbol{u}(x, \pm 0.5; t) = (\pm 1, 0), \qquad \boldsymbol{u}(\pm 0.5, y; t) = (0, \pm 1). \tag{2.2}$$

Time evolution has been performed using the Lattice–Boltzmann method (LBM) (Chen & Doolen 1998). We have adopted the 9-bit LBGK-D2Q9 lattice Boltzmann model of Qian, D'Humières & Lallemand (1992) and discretised the domain with $N = 513$ points in both spatial directions. Compressibility effects have been kept moderate by setting the lid velocity to $U = 0.1$ in LBM units. The code used was thoroughly tested and validated by An, Bergada & Mellibovsky (2019, 2020*a*,*b*,*c*) on both square and triangular cavities. No regularisation has been applied to contain the effects of the discontinuous velocity at the corners. A few test cases run with double resolution ($N = 1025$) at $Re = 500$ and 744 establish that the error in the velocity fields of steady states remains below $\varepsilon_{\boldsymbol{u}} \equiv \|\boldsymbol{u}_{513} - \boldsymbol{u}_{1025}\|/\|\boldsymbol{u}_{1025}\| < 1\ \%$, as measured with the norm defined by (2.8), and that the period of periodic solutions is accurate to within $\varepsilon_T \equiv |T_{513} - T_{1025}|/T_{1025} < 0.5\ \%$. Some additional runs with the higher resolution at varying Re approaching the heteroclinic bifurcation ($Het_{S'}$) that generates the globally attracting space–time-symmetric orbit ($C_{S'}$) bound the error in its occurrence to within $\varepsilon_{Re} \equiv |Re^{513}_{Het_{S'}} - Re^{1025}_{Het_{S'}}|/Re^{1025}_{Het_{S'}} < 0.1\ \%$. To gauge the effects of disregarding corner singularities, we have re-run the steady states and periodic orbits at the same $Re = 500$ and 744 with a double hyperbolic tangent regularisation of the wall velocity following $w(z) = \pm[\tanh(k(0.5 + z) + \tanh(k(0.5 - z)) - 1)]^2$, where k is the regularisation parameter, and $w \in \{u, v\}$, $z \in \{x, y\}$ and the $\pm$ sign are taken as required for each of the lids. The discrepancies with respect to the non-regularised case – solution norm for equilibria and period for orbits – decrease monotonically and smoothly as k is increased. The same holds true for the heteroclinic critical point at which the globally attracting periodic orbit appears, further supporting that the non-regularised cavity considered here is but the limiting case of the regularised cavity as $k \to \infty$.

The symmetry group of the problem at hand is the fourth-order dihedral group (D_2, the symmetries of a non-square rhombus or rectangle). In addition to the identity operation,

https://doi.org/10.1017/jfm.2026.11516 Published online by Cambridge University Press

the other three elements of the group are

$$M_{\backslash} : [u, v](x, y) = [-v, -u](-y, -x), \tag{2.3}$$

$$M_{/} : [u, v](x, y) = [v, u](y, x), \tag{2.4}$$

$$R_{\pi} : [u, v](x, y) = [-u, -v](-x, -y). \tag{2.5}$$

Here, M denotes mirror symmetry with respect to the northwest–southeast ($M_{\backslash}$) or southwest–northeast ($M_{/}$) diagonals; R corresponds to rotations about the cavity centre of angle 0 ($R_0 = I$, the identity) or π (R_{π}). Each element is self-inverse and commutes with any other element (the group is Abelian). Composing any two of the non-identity elements produces the third.

Point probes at $\boldsymbol{x}_T = (0, 0.25)$, $\boldsymbol{x}_L = (-0.25, 0)$ and $\boldsymbol{x}_B = (0, -0.25)$, located half-way between the origin and the top, left and bottom walls, respectively, and labelled T, L and B in figure 1, can be exploited to characterise solutions in terms of their symmetries. Symmetry $M_{\backslash}$ cancels exactly the pseudo-velocities

$$u_{\backslash} = \frac{u_T + v_L}{2} \qquad \text{and} \qquad v_{\backslash} = \frac{v_T + u_L}{2}. \tag{2.6}$$

Similarly, the pseudo-velocities

$$u_{/} = \frac{u_L - v_B}{2} \qquad \text{and} \qquad v_{/} = \frac{v_L - u_B}{2} \tag{2.7}$$

vanish for solutions that are invariant under symmetry $M_{/}$. Finally, for R_{π}-preserving solutions, we have $u_{\pi} = (u_T + u_B)/2$, $v_{\pi} = (v_T + v_B)/2$ cancel exactly.

All the solutions found and reported in the present study preserve the R_{π} symmetry such that only a Z_2 reflection symmetry, corresponding to either $M_{\backslash}$ or $M_{/}$, needs be considered in the determination of the normal form whose unfolding produces the bifurcation scenario under scrutiny. Most solutions are stable to perturbations breaking the R_{π} symmetry and can, therefore, be computed in the full phase space. Solutions unstable to R_{π} symmetry breaking perturbations have required R_{π} symmetry restricted simulations for their computation. Finally, simulations simultaneously enforcing any two of R_{π}, $M_{\backslash}$ and $M_{/}$ have also been deployed to converge the symmetric base state at values of Re for which instabilities breaking all three symmetries have already developed. There are several ways in which symmetries might be enforced. The most efficient procedure consists in working with a half-domain (bounded by two adjacent lids and a diagonal) to enforce any one of the symmetries, or a quarter-domain (one lid and two semi-diagonals issued from the corners and meeting at the centre of the cavity) to enforce all three symmetries simultaneously. The boundary conditions on the lids remain the same, while those for the diagonals are worked out from the symmetries that the distribution functions must fulfil along them. A second option, less efficient but computationally simpler, is to run on the full domain and symmetrise the flow field after every time step (or every few time steps) as required by the symmetry or symmetries being prescribed. We have used both approaches interchangeably with identical results.

Throughout this paper, either of the pseudo velocities $u_{\backslash}$ or $v_{\backslash}$ have been used to detect $M_{\backslash}$ symmetry breaking and the dynamics of the solutions have been represented through phase map on the $(u_{\backslash}, v_{\backslash})$-plane. 2-D phase map projections can be misleading in gauging the proximity of solutions in phase space. To quantify the distance between solutions and detect close approaches of phase space trajectories to steady states,

https://doi.org/10.1017/jfm.2026.11516 Published online by Cambridge University Press

it is convenient to endow the phase space with a suitable norm

$$\|\boldsymbol{u}\| = \int_{-0.5}^{0.5} \int_{-0.5}^{0.5} \sqrt{u^2 + v^2}\, \mathrm{d}x\, \mathrm{d}y \tag{2.8}$$

and then define the metric as $d(\boldsymbol{v}, \boldsymbol{u}) = \|\boldsymbol{v} - \boldsymbol{u}\|$, where $\boldsymbol{v}$ and $\boldsymbol{u}$ are two velocity fields. Finally, the instantaneous distance of a phase space trajectory, characterised by the flow field evolution $\boldsymbol{v}(x, y; t)$, to a certain equilibrium state E with flow field $\boldsymbol{u}(x, y)$ is given by

$$d_E(t) = d(\boldsymbol{v}(x, y; t), \boldsymbol{u}(x, y)) \,. \tag{2.9}$$

This is the scalar quantity we monitor to detect the closest approach of a periodic orbit to a steady solution, whose meaning is thus rendered precise.

3. Overview of the bifurcation diagram

Even if only solutions preserving the R_π symmetry are considered, the 4LDSSC problem features as many as two equilibria (E) and three limit cycles (C) inter-related by nine bifurcations. Figure 2 shows the bifurcation diagram containing all solution branches and bifurcation points that are accessible through R_π-restricted time integration in terms of $u_\backslash$ as a function of Re. Instabilities breaking the R_π invariance are not considered in the description that follows. The base, fully symmetric solution E_S (red) issues a pair of stable, asymmetric but $M_\backslash$-conjugate-symmetric E_A solution branches (blue) at a supercritical pitchfork bifurcation P_{1S} (leftmost red square). The stability lost in this first pitchfork is later recovered in a subcritical pitchfork bifurcation P_{2S} (rightmost red square) whence a second pair of E_A solution branches, this time unstable saddles, emerge. The nodal and saddle pairs of E_A branches meet in two symmetry-conjugate saddle-node bifurcations (SN_A, not shown) at higher Re that are not accessible with mere time-integration. While these solution branches and bifurcations had been previously reported in the literature (Chen *et al.* 2013), the remainder of the bifurcation diagram is new; with one notable exception, the long-period space–time symmetric periodic orbit, which was already known. Back to the E_S branch, the solution loses again stability, this time irreversibly, in an R_π-breaking supercritical Hopf bifurcation (H_S, red diamond). From the Hopf bifurcation, a stable branch of space–time-symmetric periodic orbits C_S (pink) emerges, which disappear eventually in a heteroclinic bifurcation (Het_S, pink stars) involving a symmetric collision with the two saddle E_A solutions. Meanwhile, the nodal E_A solutions remain stable and become focuses as Re is increased until the advent of two $M_\backslash$-symmetry-conjugate supercritical Hopf bifurcations (H_A, blue diamonds). From this point on, the unstable focuses are no longer traceable with time evolution. The two stable, $M_\backslash$-asymmetric but mutually symmetric cycles C_A (cyan) grow in amplitude over a short Re range (see the magnification in figure 2*b*) and become unstable in $M_\backslash$-conjugate-symmetric cyclic folds (FC_A, cyan triangles), reversing their progress towards decreasing Re. Once unstable, the C_A cycles grow large and collide with the saddle E_A solutions in mutually symmetric homoclinc bifurcations (Hom_A, cyan stars). At sufficiently high Re, a seemingly unconnected space–time-symmetric periodic orbit $C_{S'}$ (orange) of large amplitude and long period exists. As Re is decreased, however, the cycle disappears in a boundary crisis, again involving the saddle branches of E_A, in the guise of yet another heteroclinic bifurcation ($Het_{S'}$, orange stars). Here, $C_{S'}$, which is the aforementioned exception, was known (Wahba 2011), but its origin at $Het_{S'}$ had not been established.

All above-mentioned bifurcations are listed in table 1, indicating the type, bifurcating solution, critical value of the Reynolds number and imaginary part of the bifurcating

https://doi.org/10.1017/jfm.2026.11516 Published online by Cambridge University Press

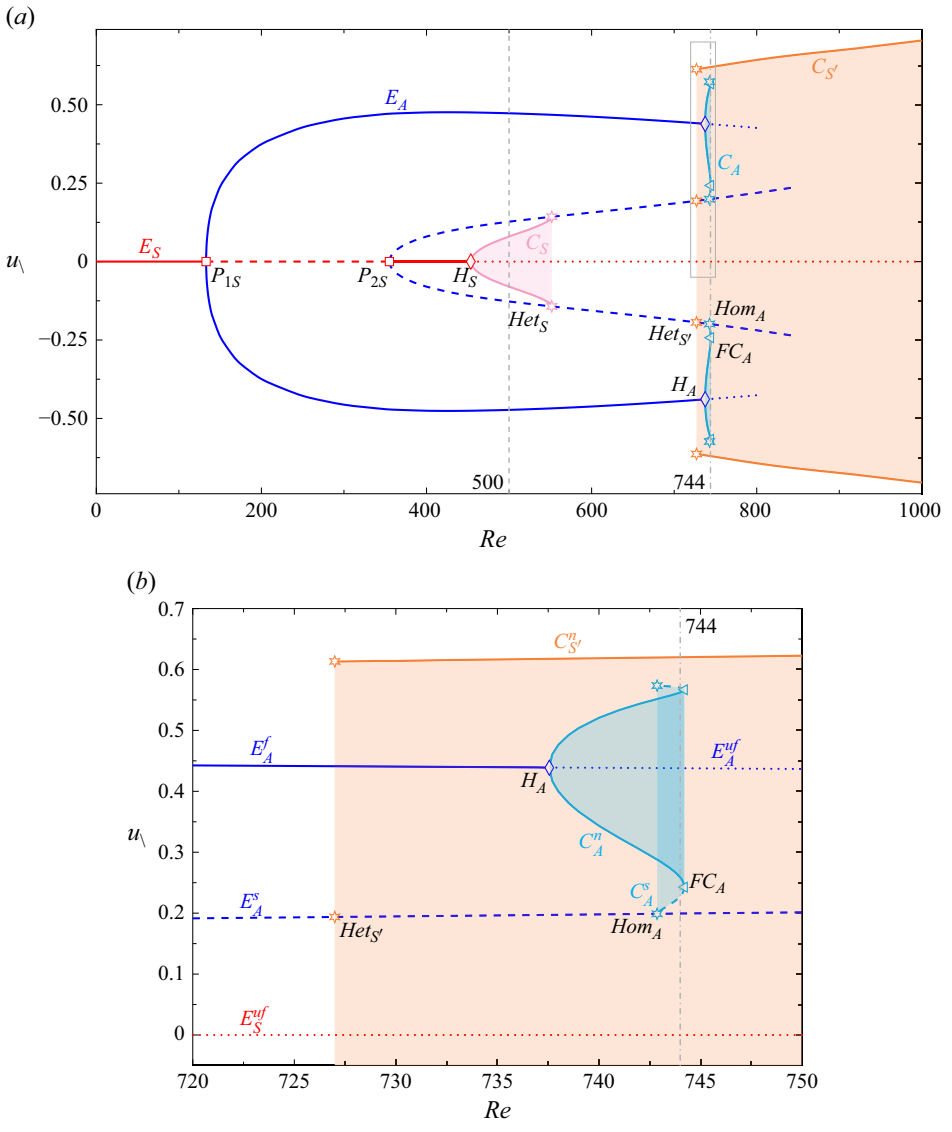


Figure 2. Bifurcation diagram for the R_π symmetry-restricted 4LDSSC flow problem. (*a*) Full diagram. Solution branches are labelled (in colour) on the top half of the diagram and bifurcations (in black) on the lower half to avoid cluttering. (*b*) Magnification of the boxed region (grey rectangle) of panel (*a*). Shown are solution branches for the symmetric E_S (red) and asymmetric E_A (blue) steady states, as well as for the space–time symmetric C_S (pink) and $C_{S'}$ (orange), and asymmetric C_A (cyan) periodic orbits. Superscripts, when present, refer to stability properties of the solution along a specific sub-branch. Line styles are assigned according to the number of unstable eigenmodes (within the R_π-restricted subspace): solid for none (node or focus, superscripts *n* or *f*), dashed for one (saddle, superscript s), dotted for two (unstable focus, superscript uf). Note that the sub-branch E_A^{uf} cannot be computed with time-evolution and has been extrapolated from E_A^f to guide the eye. Pitchfork (*P*, squares), Hopf (*H*, diamonds), fold of cycles (*FC*, triangles) and homo/heteroclinic bifurcations (*Hom*/*Het*, stars) are indicated and labelled. The subscript indicates the bifurcating solution and a numeral is used when more than one bifurcation of the same type has been identified along a branch. The solutions shown in figures 3, 4 and 5 correspond to $Re = 500$ (grey dashed line) and those in figures 6, 7, 8 and 9 to $Re = 744$ (grey dash-dotted line).

https://doi.org/10.1017/jfm.2026.11516 Published online by Cambridge University Press

Name	Type	Solution	Re	λ_i	Observations
P_{1S}	Pitchfork	E_S	132.974 ± 0.002	0	Breaks the $M_\backslash$ symmetry
P_{2S}	Pitchfork	E_S	355.05 ± 0.02	0	Breaks the $M_\backslash$ symmetry
H_S	Hopf	E_S	453.6766 ± 0.0004	0.49352 ± 0.00002	Breaks the $M_\backslash$ symmetry
Het_S	Heteroclinic	C_S	551.73366 ± 0.00006	—	Boundary crisis involving E_A
H_A	Hopf	E_A	737.554 ± 0.002	0.19182 ± 0.00002	Along with $M_\backslash H_A$
FC_A	Fold of cycles	C_A	744.193 ± 0.002	0	Along with $M_\backslash FC_A$
$Het_{S'}$	Heteroclinic	$C_{S'}$	726.9916 ± 0.0004	—	Boundary crisis involving E_A
Hom_A	Homoclinic	C_A	742.8643 ± 0.0002	—	Boundary crisis involving E_A, Along with $M_\backslash Hom_A$
SN_A	Saddle-node	E_A	?	0	Along with $M_\backslash SN_A$, Inaccessible

Table 1. List of R_π-invariant bifurcations of the 4LDSSC problem. Given are the name and type of the bifurcation, the solution concerned, the critical Re and the imaginary part of the bifurcating eigenmode. Additionally, the symmetry broken for symmetry-breaking bifurcations or the saddle solution responsible for the boundary crisis in the case of global bifurcations are provided in the Observations column. The errors have been estimated from the variance of fitting parameters as twice the standard deviation (95 % confidence interval). Note that they do not express the uncertainty associated with the numerical discretisation of the problem.

eigenvalue, along with additional observations as required. We will argue later that, provided the R_π rotational symmetry is preserved (either naturally or enforced), the full dynamics of the 4LDSSC problem is encoded in the 2-D normal form of a degeneration of the double zero bifurcation subject to Z_2 symmetry. Accordingly, only two modes are at stake, and the type and stability of the solutions are dictated by the real or complex nature of the eigenmodes as well as the sign of the real part of the respective eigenvalues λ in the case of equilibria or the modulus of the only relevant multiplier μ in the case of cycles. We will use superscripts to classify steady states as stable node (n: two negative real eigenvalues), stable focus (f: a complex pair of eigenvalues with negative real part), saddle (s: a negative and a positive real eigenvalues), unstable node (un: two positive real eigenvalues) or unstable focus (uf: a complex pair with positive real part). Similarly, limit cycles will be denoted as nodal (n: dominant multiplier within the unit circle) or saddle (s: dominant multiplier outside of the unit circle). The superscripts will be omitted when referring to the full solution branch, regardless of stability. It must be borne in mind that this stability classification concerns only the R_π invariant subspace. For instance, we will refer to C_S as a stable/nodal cycle, although it is actually linearly unstable to a R_π-breaking mode.

The symmetries of the problem imply that all R_π-preserving solutions breaking the $M_\backslash$ invariance must, of necessity, break also $M_/$. Further, solutions breaking the mirror symmetry appear in pairs, mutually related by reflection about either of the diagonals, and so do the bifurcations they undergo. All flow fields and bifurcation analyses of non-mirror-symmetric solutions will be presented throughout the paper for the $u_\backslash < 0$ version of the pair, the other being accessible through mirror reflection.

https://doi.org/10.1017/jfm.2026.11516 Published online by Cambridge University Press

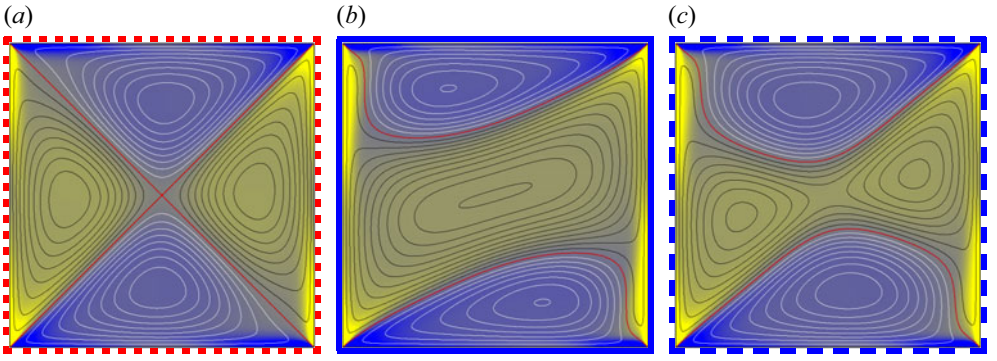


Figure 3. Steady states at $Re = 500$: (*a*) symmetric E_S^{uf}, (*b*) asymmetric focus E_A^f and (*c*) asymmetric saddle E_A^s. Shown are vorticity $\omega_z = \partial_x v - \partial_y u \in [-2.5, 2.5]$ colourmaps (blue for negative, yellow for positive) and streamfunction ψ contours (black for positive, white for negative; the zero contour in red), equispaced in steps $\Delta\psi = 0.01$. The frame denotes solution (colour) and stability within the R_π symmetry subspace (linestyle: solid for zero-dimensional unstable manifold, dashed for 1-D, dotted for 2-D).

4. Invariant solutions

In this section, we discuss all invariant solutions of the problem mainly in terms of symmetries and flow physics as regards the topology and dynamics of large-scale vortical structures within the cavity. For an extended discussion on jet dynamics and wall boundary layers, we refer the reader to Appendix A, where all exact solutions are revisited with the focus set on kinetic energy fields and wall shear stress distributions.

The base solution is a steady state that has all the symmetries of the problem and exists for all values of the Reynolds number. Figure 3(*a*) depicts vorticity (ω_z) colourmaps and streamfunction (ψ) contours for the symmetric steady state E_S at $Re = 500$. The R_π symmetry is clear from the π-rotational invariance of both ψ and ω_z, while the $M_\backslash$ and $M_/$ symmetries are evinced by the sign inversion of ψ and ω_z upon reflection with respect to either of the cavity diagonals. As a result of the aforementioned symmetries, the flow is exactly quiescent in the centre of the cavity, whence four straight streamlines are issued symmetrically along the diagonals towards the four corners. These streamlines divide the cavity into four triangular recirculation cells that do not exchange fluid. The cells adjacent to the top and bottom (left and right) walls rotate clockwise (counter clockwise) dragged by their sliding motion. Symmetric ejections of vorticity can be observed from the top-right and bottom-left corners along the diagonal, which are due to the confluence of contiguous lids running into each other. The two jets (see Appendix A) meet at the centre of the cavity along the diagonal and collide head-on preserving all symmetries. The E_S solution depicted at $Re = 500$ is unstable, but the instability being associated with a mode that breaks the $M_\backslash$ and $M_/$ invariance, enforcing either of the symmetries, along with R_π, allows computation of the state with just a time stepping code. Actually, enforcing the R_π symmetry is also necessary to stabilise E_S^{uf} beyond $Re \gtrsim Re_{P_{2S}}$ due to an R_π-breaking pitchfork bifurcation occurring very shortly after P_{2S} (see Meseguer *et al.* 2024).

Figure 4 shows a phase map representation, on the $(u_\backslash, v_\backslash)$ plane, of the 4LDSSC problem at $Re = 500$. The symmetric solution E_S^{uf} of figure 3(*a*) appears in this depiction as a point at the origin (red empty circle). The R_π-restricted time evolution starting from its immediate vicinity spirals away (grey lines), revealing its nature as an unstable focus, i.e. having a complex-conjugate pair of unstable modes, hence the superscript.

https://doi.org/10.1017/jfm.2026.11516 Published online by Cambridge University Press

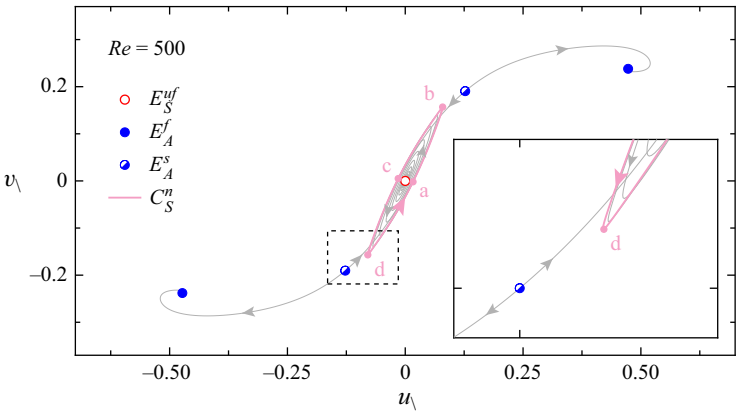


Figure 4. Phase map projection, on the $(u_\backslash, v_\backslash)$ plane, at $Re = 500$. Steady states are represented with circles, the pattern (filled, half-filled or empty) denoting the dimensionality of the unstable manifold (null, one or two) within the R_π subspace. Colour lines closing in loops represent limit cycles (solid for stable, dashed for unstable). Grey lines are connecting manifolds approximated by time evolution. Arrow heads indicate time direction. Labelled bullets indicate snapshots in figure 5. The region within the box has been enlarged in the inset.

At sufficiently low values of the Reynolds number ($Re < Re_{P_{1S}}$), E_S^n is stable and, being the only stable state, acts as a global attractor. In this regime, the solution may be converged in the full square domain without enforcing any of its symmetries. The stability is lost in a supercritical pitchfork bifurcation P_{1S} at $Re_{P_{1S}} \simeq 133.0$, whence a pair of symmetry-conjugate branches of stable nodal asymmetric states E_A^n are issued that eventually evolve into stable focuses E_A^f in a node-focus transition. At the transition, the leading eigenvalue of E_A^n, which is real and stable, collides with a second real eigenvalue and together form a complex pair. As a result, trajectories cease to approach the solution monotonically and start spiralling instead. The stable node E_A^n becomes a stable focus E_A^f, with no change in its stability, and no new solutions are created either. The transition is not a bifurcation and is therefore not shown in figure 2(*a*), where E_A^n and E_A^f are two consecutive portions of the stable E_A sub-branch (solid blue). Here, E_A^f, shown in figure 3(*b*) at $Re = 500$, preserves the R_π invariance, but breaks both the $M_\backslash$ and $M_/$ symmetries. As already pointed out, there exist two $E_A^{n/f}$ states which are symmetry conjugates of one another. The state conjugate to that shown in figure 3(*b*) may be obtained from it by applying either of the broken reflection symmetries to E_A: $M_\backslash E_A = M_/ E_A$. It may also be obtained from time evolution in the full square domain, without applying any symmetry restriction, but starting from an appropriate choice of initial condition. For E_A^f, the jets, shy of colliding at the cavity centre, deviate from the diagonal to one side and the other (see Appendix A). As a result, the jets avoid mutual collision, but impinge on opposite walls instead – opposite from the vertex whence the jets are issued and opposite from one another to avoid crossing. Two of the isolated recirculation regions bounded by opposing walls that were characteristic of E_S have merged across the cavity centre into one large vortex, while the other two remain separate and have shrunk on account of their having been pushed towards their respective walls. In the phase map projection of figure 4, the two symmetry-conjugate E_A^f states (filled blue circles) are related by a 180° rotation about the origin. They are stable focuses, as indicated by the inward spiralling behaviour of their stable manifold (grey oriented lines).

https://doi.org/10.1017/jfm.2026.11516 Published online by Cambridge University Press

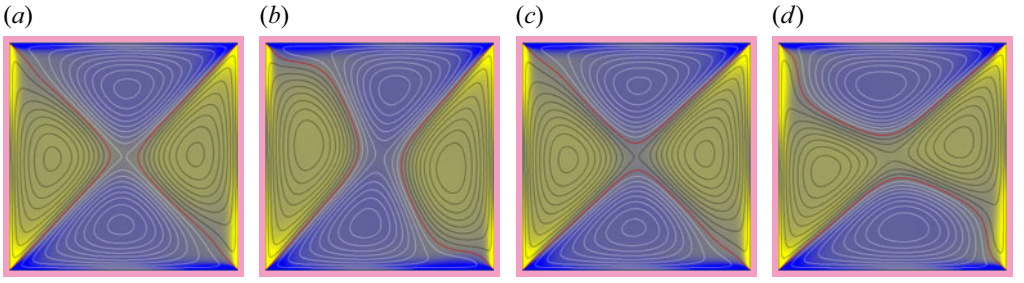


Figure 5. Space–time symmetric periodic orbit C_S at $Re = 500$. Snapshots of the solution at (*a*) t_0, (*b*) $t_1 = t_0 + 3.32$ (closest approach to $M_{\backslash}E_A^s$), (*c*) $t_2 = t_0 + T/2$, (*d*) $t_3 = t_1 + T/2$ (closest approach to E_A^s), corresponding to the labelled bullets in figure 4. The period of the solution is $T = 15.321$. Styles as for figure 3.

In addition to E_A^f and $M_{\backslash}E_A^f$, R_π-restricted time evolution at $Re = 500$ occasionally converges on a third instance of stable invariant solution in the form of a space–time symmetric cycle C_S, four snapshots of which are shown in figure 5 (see supplementary movie 1 available at https://doi.org/10.1017/jfm.2026.11516). Unlike E_S and E_A, which were already known (Chen *et al.* 2013), the cycle C_S is reported here for the first time. The cycle can be traced back in Re to a Hopf bifurcation H_S of E_S that breaks both the $M_{\backslash}$ and $M_{/}$ symmetries at $Re_{H_S} \simeq 453.7$, and also forward until its annihilation in a heteroclinic bifurcation Het_S at $Re_{Het_S} \simeq 551.7$ involving E_A states. In addition to the time invariance TP of periodic orbits to evolution over a full period T,

$$TP : [u, v](x, y; t) = [u, v](x, y; t + T), \tag{4.1}$$

C_S possesses also a space–time symmetry ST that makes it also invariant under evolution over a half-period $T/2$ followed by reflection with respect to any of the two diagonals:

$$ST : [u, v](x, y; t) = [v, u](y, x; t + T/2) = [-v, -u](-y, -x; t + T/2). \tag{4.2}$$

The ST symmetry is apparent from comparing pairs of snapshots exactly $T/2$ apart. figure 5(*c*) at time $t_0 + T/2$ and figure 5(*d*) at $t_1 + T/2$ are the $M_{\backslash}$ (and $M_{/}$) mirror images of figure 5(*a*) at t_0 and figure 5(*b*) at $t_1 = t_0 + 3.32$, respectively. As for E_A, the instantaneous flow topology of C_S consists of two impermeable R_π-related vortices attached to two facing walls and a large region connecting the other two walls across the centre of the cavity. The dynamics, however, generate a dislocation every half-period at the very centre of the cavity that merges the extant two separate vortices into a new large connected region and, by so doing, splits the old domain-crossing region into two separate vortices. Unlike E_A, which avoided the collision of the jets at the cavity centre permanently, C_S accomplishes the same end dynamically by having the jets oscillate about the diagonal in phase opposition (see Appendix A). One bends up and the other down in an alternated fashion – or, equivalently, both clockwise, then anticlockwise. In the phase map projection of figure 4, the stable (stable in the R_π invariant subspace, that is, hence the superscript n) cycle C_S^n shows as a π-rotational symmetric closed loop (solid pink line) around E_S^{uf}, from which it has bifurcated. Indeed, the unstable manifold of the latter state drives the dynamics directly to the former. Incidentally, figures 5(*a*) and 5(*c*) are the mutually symmetric closest approaches to the vicinity of E_S, occurring shortly after the back and forth vortex rearrangements, while figures 5(*b*) and 5(*d*) are closest visits to the two mutually symmetric branches of an unstable asymmetric steady state that we shall discuss presently.

https://doi.org/10.1017/jfm.2026.11516 Published online by Cambridge University Press

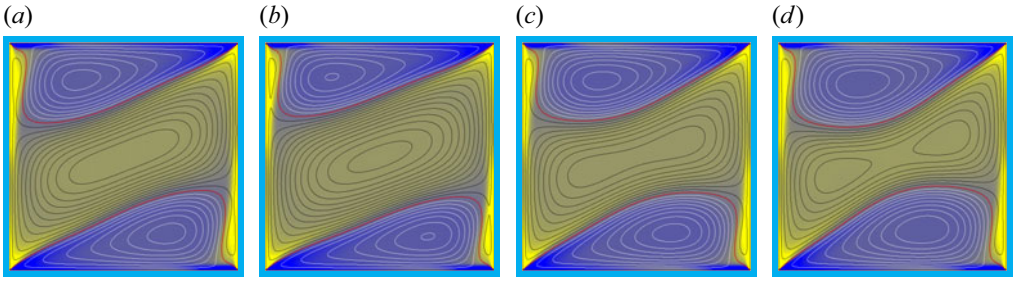


Figure 6. Asymmetric periodic orbit C_A^n at $Re = 744$. Snapshots of the solution at (*a*) t_0, (*b*) $t_1 = t_0 + 5.08$, (*c*) $t_2 = t_0 + 15.63$ and (*d*) $t_3 = t_0 + 26.17$ (closest approach to E_A^s), corresponding to the labelled bullets in figure 7. The period of the solution is $T = 37.432$. Styles as for figure 3.

The coexistence of more than one local attractor at $Re = 500$ suggests that a phase space threshold must be in place that separates the respective basins of attraction. A useful tool to study the basin boundary with nothing but a time stepping code is the edge tracking algorithm (Itano & Toh 2001; An *et al.* 2019). In our case, the shoot-and-refine process has been applied to initial conditions generated by linear interpolation between the flow fields of E_A^f and those of an arbitrary snapshot of C_S. Successive refinement iterations have the transient dynamics approach, for increasingly longer lapses, a saddle steady state E_A^s, whose flow field is shown in figure 3(*c*). While the topology of the solution coincides with that of E_A^f, the actual flow field is half-way between those of E_S^{uf} and E_A^f. As all R_π-invariant non-mirror-symmetric solutions, E_A^s comes also in symmetry-conjugate pairs, mutually related by both the $M_\backslash$ and $M_/$ mirror symmetries. The new branch can be traced back in Re, duly switching to edge tracking between E_S^n and E_A^f below Het_S, to a subcritical symmetry-breaking pitchfork bifurcation P_{2S} of E_S that breaks both $M_\backslash$ and $M_/$ at $Re_{P_{2S}} \simeq 355.1$. Forward continuation via edge tracking beyond Het_S requires trading the C_S snapshot for E_S^{uf} and bisecting between trajectories going back to either E_A^f or its mirror image.

According to Chen *et al.* (2013) and Meseguer *et al.* (2024), the saddle branch E_A^s coalesces at even higher Re in a saddle-node bifurcation with the unstable nodal branch E_A^{uf}. Signs of the approach to the saddle-node bifurcation SN_A are apparent from the increasing slope of the branch in figure 2(*a*), but the divergingly slow dynamics in the vicinity of saddle-node bifurcations and the inability of time evolution to converge the asymmetric unstable focus hinder the precise determination of its occurrence. A steady-state solver would be required to analyse SN_A properly.

The stable asymmetric focus E_A^f may be continued in Re with the time stepper up to a supercritical Hopf bifurcation H_A, beyond which point it becomes an unstable focus E_A^{uf} and is inevitably lost to time evolution codes (shown in figure 2 as the prolongation of the E_A^f branch beyond the H_A point, approximated by extrapolation). Two R_π-invariant, $M_\backslash$- and $M_/$-breaking (but symmetry-conjugate) stable limit cycles C_A^n and $M_\backslash C_A^n$, replace E_A^f and $M_\backslash E_A^f$ in their role as attractors. Neither the H_A point nor the resulting pair of cycles has been reported elsewhere. Four snapshots of C_A^n are shown in figure 6 (see supplementary movie 2) at $Re = 744$. The flow topology is the same as for the two E_A branches, nodal and saddle, at all times, but while the flow field resembles $\mathrm{E}_A^{n/f}$ (i.e. the stable E_A, be it node or focus) over the best part of a period (compare figures 6*a*–6*c* with figure 8*h*), the solution conspicuously approaches E_A^s once every period (see figure 6*c*

https://doi.org/10.1017/jfm.2026.11516 Published online by Cambridge University Press

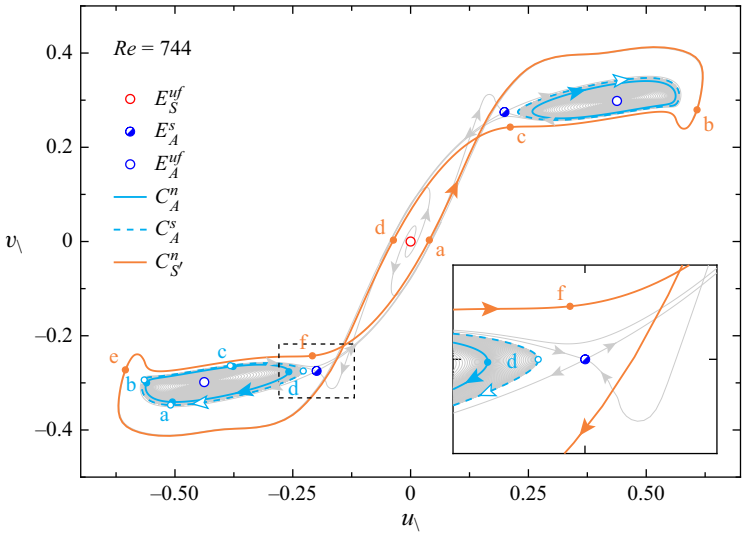


Figure 7. Phase map projection at $Re = 744$. Styles as for figure 4. The location of E_A^{uf} has been quadratically extrapolated from the stable focus E_A^f at $Re = 735$, 736 and 737. Labelled bullets indicate snapshots in figures 6, 8 and 9. The region within the box has been enlarged in the inset.

for the closest approach, to be compared with figure 8*i*). The jets configuration is similar to that for E_A^{uf}, but the impingement point on the walls oscillates around the equilibrium position (see Appendix A).

If the C_A^n branch is bounded from below by the Hopf bifurcation H_A from which it springs at $Re_{H_A} \simeq 737.6$, neither can it be continued beyond a fold of cycles FC_A occuring very shortly after at $Re_{FC_A} \simeq 744.2$.

Figure 7 depicts the phase map portrait of the 4LDSSC problem at $Re = 744$. All steady states of figure 4 are still present, but while E_S^{uf} (red blank circle) and E_A^s (blue half-filled circle) are still an unstable focus and an unstable saddle, respectively, E_A^f has turned into an unstable focus E_A^{uf} (blue blank circle). As an asymmetric unstable focus, E_A^{uf} can neither be reached through time evolution nor by edge tracking, so its location has been approximated through quadratic extrapolation of the stable focus E_A^f at neighbouring values of the Reynolds number, i.e. $Re = 735$, 736 and 737. The pair of C_A^n cycles (solid cyan lines) show as two closed loops related by a 180° rotation about the origin. Each revolves around one of the mutually symmetric E_A^{uf} states and seemingly approaches, once every period, the nearmost E_A^s state.

Even though C_A^n and its mirror-symmetric counterpart are stable at $Re = 744$, time evolution initialised from the symmetric base state E_S^{uf} is eventually seized by yet another stable limit cycle $C_{S'}$. This periodic orbit, a few snapshots of which are shown in figure 8(*a–f*) (see supplementary movie 3), has the same flow topology and space–time symmetry ST of C_S, but with significantly longer period. Its amplitude is also substantially larger. Also shown, for reference, are the flow fields of E_S^{uf} (figure 8*g*), computed through time stepping by enforcing all problem symmetries, an approximation to E_A^{uf} (figure 8*h*), quadratically extrapolated from E_A^f at the neighbouring $Re = 735$, 736 and 737, and E_A^s (figure 8*i*), obtained via edge tracking bewteen arbitrary snapshots of C_A^n and $C_{S'}$, bisecting

https://doi.org/10.1017/jfm.2026.11516 Published online by Cambridge University Press

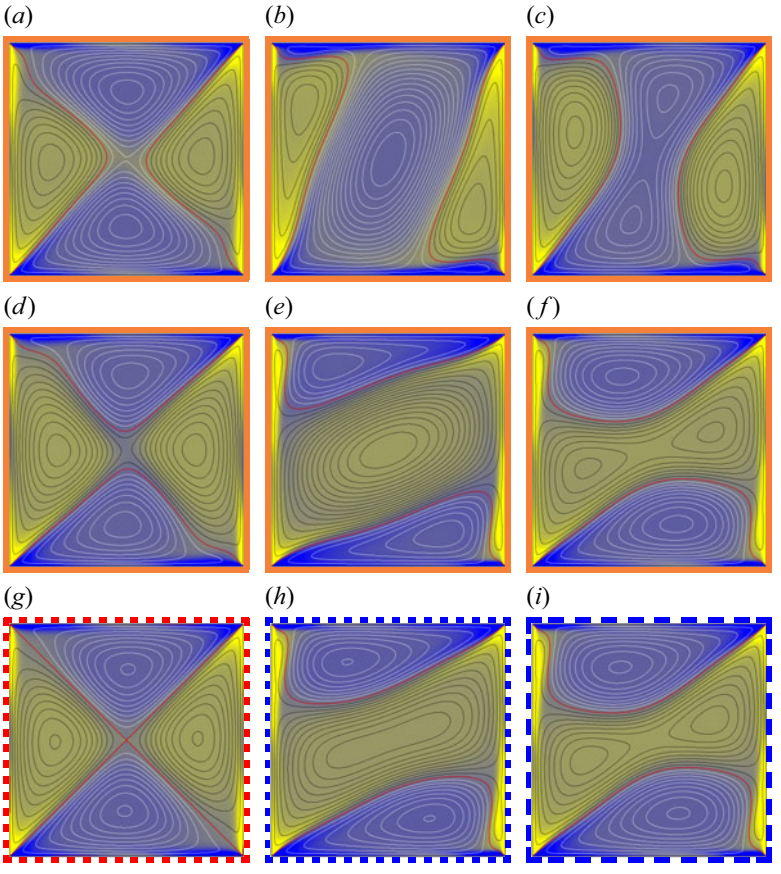


Figure 8. (*a–f*) Space–time symmetric periodic orbit $C^n_{S'}$ at $Re = 744$, together with steady states (*g*) E^{uf}_S, (*h*) E^{uf}_A (quadratically extrapolated from E^f_A at $Re = 735$, 736 and 737) and (*i*) E^s_A. Snapshots of $C^n_{S'}$ are taken at (*a*) t_0, (*b*) $t_1 = t_0 + 7.42$, (*c*) $t_2 = t_0 + 26.5$ (closest approach to $M_\backslash E^s_A$), (*d*) $t_3 = t_0 + T/2$, (*e*) $t_4 = t_1 + T/2$, (*f*), $t_5 = t_2 + T/2$ (closest approach to E^s_A), corresponding to the labelled bullets in figure 7. $T = 66.338$ is the period of the solution. Styles as for figure 3.

between trajectories following two different paths to $C_{S'}$. While C_S orbited in the vicinity of E_S with alternate periodic approaches to E^s_A and its mirror image, $C_{S'}$ reaches further and revolves in turns around E^{uf}_A and its symmetric (compare the flow fields of figures 8*b*,e with figure 8*h*). At other times, the trajectory evolves in the close neighbourhood of E_S (compare the flyby in figures 8*a* and 8*d*, just after the merging/splitting of vortex pairs across the cavity centre, with figure 8*g*) and twice every period approaches within a very short distance of $M_\backslash E^s_A$ and E^s_A (see figures 8*c* and 8*f*, to be compared with figure 8*i*). The cycle $C_{S'}$ can be traced back to a heteroclinic bifurcation $Het_{S'}$ at $Re_{Het_{S'}} \simeq 727.0$ and forward to Reynolds numbers in excess of $Re > 1000$, still retaining its stability and having become the sole attractor of the 4LDSSC problem from FC_A onwards, and the sole non-trivial solution beyond the surmised SN_A. This orbit, whose dynamics reconnect the two $M_\backslash$-symmetry related halves of phase space, is the one responsible for the onset of chaos at larger Re.

The seeming occurrence of a fold of cycles suggests at once that the stable branch C_A must be turning towards lower Re and, therefore, that the nodal cycle C^n_A must be shielded by a saddle cycle C^s_A. Such an unstable periodic orbit should, in principle, attract the

https://doi.org/10.1017/jfm.2026.11516 Published online by Cambridge University Press

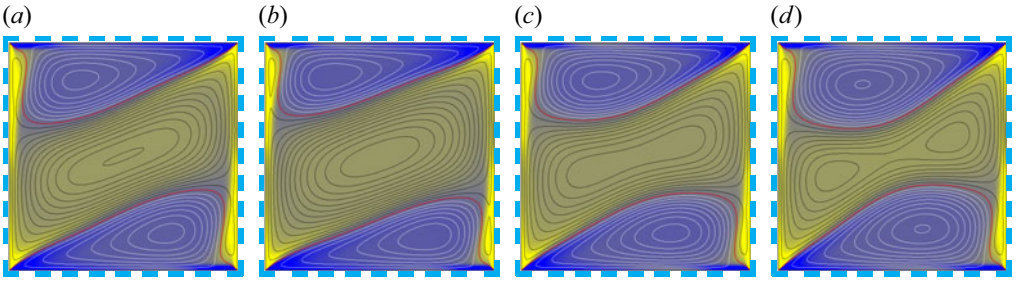


Figure 9. Asymmetric periodic orbit C_A^s at $Re = 744$. Snapshots of the solution at (*a*) t_0, (*b*) $t_0 + 5.27$, (*c*) $t_0 + 15.23$, (*d*) $t_0 + 29.18$ (closest approach to E_A^s), corresponding to the labelled bullets in figure 7. The period of the solution is $T = 42.070$. Styles as for figure 3.

dynamics on the basin boundary separating the two coexisting stable solutions C_A^n and $C_{S'}$ and would, therefore, be accessible by edge tracking between any two instantaneous flow fields, each taken from one of the two attractors. Indeed, the edge tracking procedure at $Re = 744$ produces an unstable limit cycle C_A^s, portrayed in figure 9 (see supplementary movie 4). The proximity in phase space makes this saddle periodic orbit very similar to the nodal cycle C_A^n, but the flow field differences can still be detected with the naked eye, particularly when comparing well-defined analogous instants, such as their respective closest approaches to E_A^s (see figures 9*d* and 6*d*). The C_A^s branch, issued backwards from FC_A, is short and dies in a homoclinic bifurcation Hom_A at $Re_{Hom_A} \simeq 742.9$. Needless to say, the branch and bounding bifurcations have all their mirror-symmetric counterparts.

5. Phase portraits

All exact R_π-invariant solutions of the 4LDSCC problem are contained between the phase portraits at $Re = 500$ (figure 4) and $Re = 744$ (figure 7). We now turn our attention to the various phase map topologies that succeed one another as the Reynolds number is increased from very low up to $Re \leq 1000$. Figure 10 shows all structurally stable phase portraits, in addition to those presented earlier in figures 4 and 7 for illustration purposes, in order of increasing Re. At $Re = 100$ (figure 10*a*), the symmetric state E_S^n is the sole exact solution and, as such, acts as a global attractor. At $Re = 300$ (figure 10*b*), the symmetric state E_S^s has become a saddle and is flanked at either side of its stable manifold by a pair of $M_\backslash$-conjugate E_A^f, now the only attractors of the problem. Incidentally, the states had been stable nodes E_A^n for some Re-range after their bifurcation, but they have already become focuses in a non-bifurcation node–focus transition by the time $Re = 300$ is reached. The unstable manifold (grey lines) of E_S^s points directly towards E_A^f, the final approach following a spiralling trend that is barely noticeable at this value of Re. At $Re = 360$ (figure 10*c*), the symmetric state has recovered its former stability (as long as the R_π invariance is enforced) and a second pair E_A^s of asymmetric states, now saddles, have appeared. The unstable manifolds of these new states point on one side towards the symmetric state E_S^n and on the other to the closest asymmetric stable state E_A^f, now more clearly a focus. At $Re = 425$ (figure 10*d*), the symmetric state E_S^f has also undergone a node-focus transition (compare its stable manifold in the insets). At $Re = 500$ (see figure 4), the symmetric state has destabilised anew and become an unstable focus E_S^{uf}, while a new attractor, in the form of a space–time symmetric cycle C_S collects the dynamics issued from E_S^{uf} or from the side of the unstable manifold of E_A^s

https://doi.org/10.1017/jfm.2026.11516 Published online by Cambridge University Press

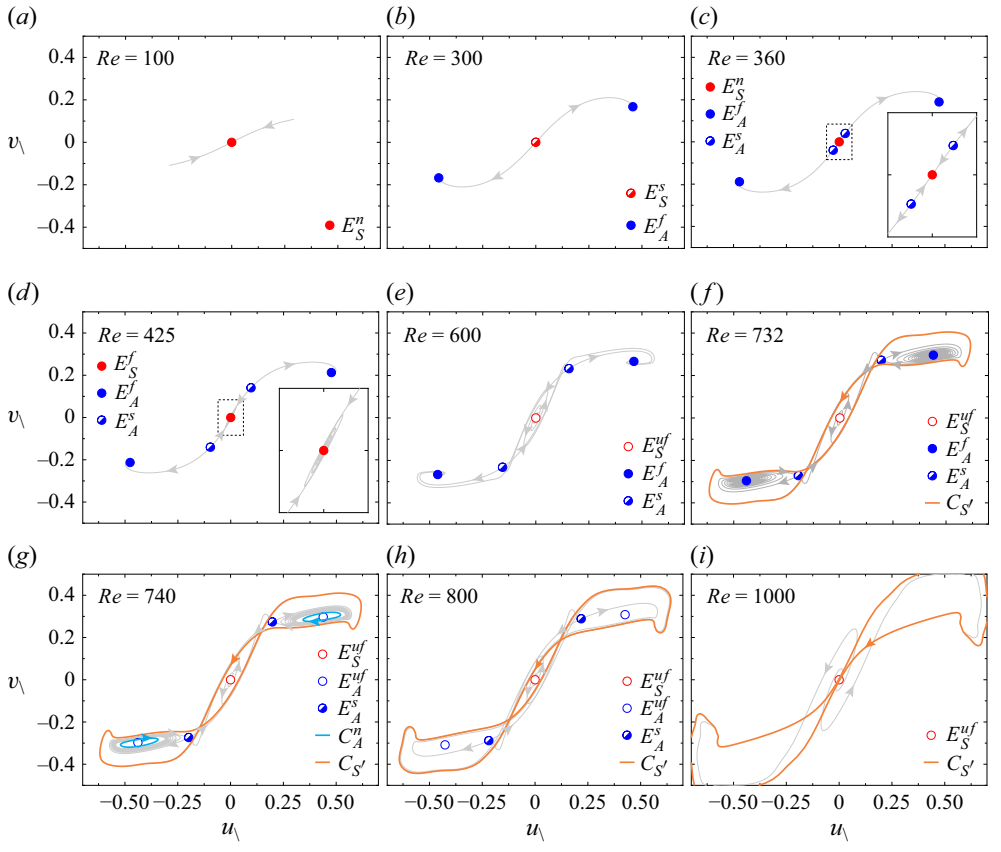


Figure 10. Phase portraits of the 4LDSSC problem at (*a*) $Re = 100$, (*b*) 300, (*c*) 360, (*d*) 425, (*e*) 600, (*f*) 732, (*g*) 740, (*h*) 800 and (*i*) 1000. Styles as for figure 4.

that pointed towards E^f_S at lower Re. At $Re = 600$ (figure 10*e*), the cycle C_S has vanished into thin air, the phase space region it enclosed has opened and trajectories issued from the neighbourhood of E^{uf}_S are now free to reach the only surviving attractors, the pair E^f_A. At $Re = 732$ (figure 10*f*), a new stable space–time symmetric cycle $C_{S'}$ orbiting around all other existing solutions has come into existence. All trajectories issued from the vicinity of E^{uf}_S, and from most of the phase space, are driven towards $C_{S'}$. The stable and unstable manifolds of E^s_A divide its neighbourhood into four quadrants, three of which belong to the basin of attraction of $C_{S'}$, while the fourth pushes trajectories towards E^f_A. At $Re = 740$ (figure 10*g*), this asymmetric pair of solutions have become unstable focuses E^{uf}_A and trajectories starting from their neighbourhood converge onto the nearest of the two stable asymmetric limit cycles C^n_A, mutually related by the $M_\backslash$-symmetry. At $Re = 744$ (see figure 7), a pair of saddle cycles C^s_A have emerged that surround either cycle of the pair C^n_A. The stable cycles are effectively shielded by the saddle cycles, so that the former are no longer reachable from the vicinity of E^s_A and the full phase space, with exception of the region enclosed within C^s_A, which remains drawn towards C^n_A, becomes the basin of attraction of $C_{S'}$. At $Re = 800$ (figure 10*h*), the cycles C^n_A and C^s_A have collided in pairs and disappeared altogether, leaving $C_{S'}$ as the sole and, therefore, global attractor and the full phase space as its basin of attraction. Finally, at $Re = 1000$ (figure 10*i*), the asymmetric

https://doi.org/10.1017/jfm.2026.11516 Published online by Cambridge University Press

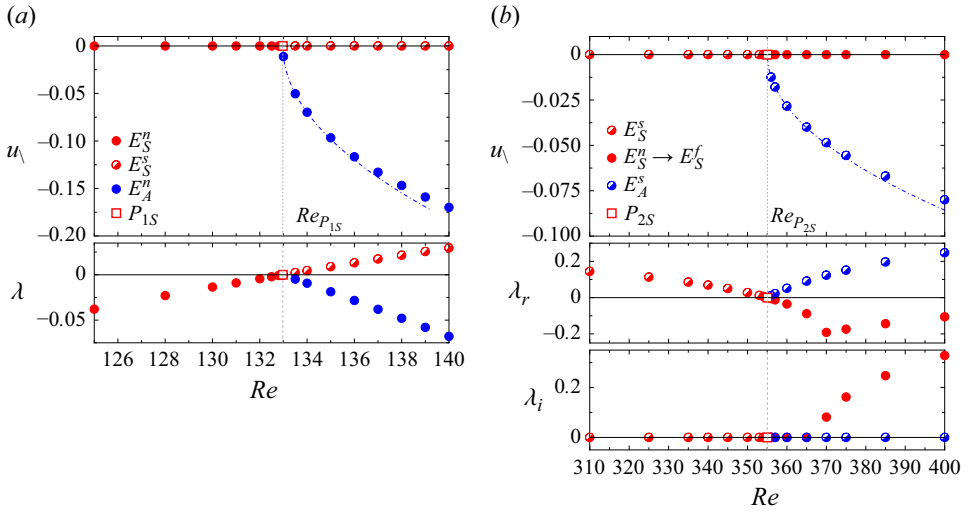


Figure 11. Pitchfork bifurcations of the R_π, $M_\backslash$- and $M_/$-symmetric base state E_S, breaking the $M_\backslash$ and $M_/$ invariance. The symmetry parameter $u_\backslash$ and the bifurcating eigenvalue $\lambda = \lambda_r + \mathrm{i}\lambda_i$ are monitored as a function of Re. (*a*) Supercritical pitchfork bifurcation P_{1S} (here, $\lambda_i = 0$ so that $\lambda = \lambda_r$ over the full Re-range considered). (*b*) Subcritical pitchfork bifurcation P_{2S}. Square-root fits to locate the pitchfork points are indicated with dash-dotted lines.

saddle E_A^s and nodal E_A^{un} steady states, the latter having, at some point, transitioned into unstable nodes, have collided in pairs and vanished. The cycle $C_{S'}$ is not only a global attractor, but also the only remaining non-trivial invariant solution, exception made, of course, of the unstable base state E_S^{utf}. Shortly after, at slightly higher Re, $C_{S'}$ is succeeded by a chaotic attractor (not shown).

6. Analysis of bifurcations

Except for the (non-bifurcation) node-focus transition occurring between figures 10(*c*) and 10(*d*), all other Re-consecutive phase portraits of figures 4, 7 and 10 are mediated by bifurcations, either local or global. In this section, we investigate the nature of each of these bifurcations and analyse them to the extent that is feasible with time integration only. Details of the stability analysis methodology can be found in Appendix B. All bifurcations and the phase space topology alterations they induce will be revisited in § 7 with the aid of phase portrait sketches to place them in context.

6.1. *Local bifurcations*

From $Re = 100$ to 300 (figures 10*a* and 10*b*), the base state E_S becomes unstable and the pair of $M_\backslash$-related stable equilibria E_A^n emerge. The scenario is suggestive of a pitchfork bifurcation and figure 11(*a*) confirms it, while revealing, at the same time, its supercritical nature. The quantity $u_\backslash$ has been used to monitor the degree of disymmetry of the steady states E_A as a function of Re. A square root fit of the form

$$u_\backslash^{fit} = u_\backslash^1 \sqrt{Re - Re_{P_{1S}}} \tag{6.1}$$

to the leftmost E_A^n points substantiates the supercritical nature of the pitchfork bifurcation P_{1S} and establishes its occurrence at $Re_{P_{1S}} = 132.974 \pm 0.002$, in fair agreement with previously reported values (Wahba 2009; Cadou *et al.* 2012; Chen *et al.* 2013).

https://doi.org/10.1017/jfm.2026.11516 Published online by Cambridge University Press

The leading eigenvalue λ has been estimated, at each value of Re, from exponential fits to the linear regime of the $v_\backslash$ time series in their final approach to (initial departure from) the stable (unstable) state, having previously discarded, for unstable solutions, the very first initial transients on account of multimodality (see Appendix B). The unstable E_S^s has been converged by enforcing $M_\backslash$ in the time stepper. As expected for a supercritical pitchfork bifurcation, the leading eigenvalue λ of the bifurcating solution E_S is real and crosses the imaginary axis precisely at the bifurcation point, while that of the bifurcated solution E_A^n debuts with zero real part and evolves towards negative values.

A second pitchfork bifurcation P_{2S} may be conjectured between $Re = 300$ and 360 (figures 10*b* and 10*c*). The symmetric base state E_S recovers stability to $M_\backslash$ perturbations, while a second pair of $M_\backslash$-related equilibria E_A^s, this time unstable, pop into existence. Incidentally, the base state is only really stable if the R_π symmetry is specifically enforced. Otherwise, phase map trajectories are apt to escape it by temporarily violating the R_π invariance, although the symmetry is eventually recovered later on upon their final approach to either of the stable E_A^f evolved from the E_A^n pair bifurcated at P_{1S}. The pair E_A^f is, therefore, globally stable when considered in the full phase space. The added instability is the result of a third pitchfork bifurcation P_{3S}, almost coincidental with P_{2S}, this time breaking the R_π symmetry (Meseguer *et al.* 2024). We will not be concerned here with instabilities disrupting the R_π invariance of the 4LDSSC problem. The analysis of P_{2S}, analogous to that of P_{1S}, is illustrated in figure 11(*b*). While the unstable E_S^s have been obtained by enforcing the $M_\backslash$ symmetry in the time evolution, the saddle E_A^s solutions have required R_π-restricted edge tracking between the base state $E_S^{n/f}$ and one of the stable E_A^f, now already stable focuses. Because of the R_π-breaking pitchfork bifurcation P_{3S} and a closely related R_π-breaking pitchfork P_A on the E_A^s branch, the whole bifurcation analysis for P_{2S} must be done on the R_π-invariant subspace. Imposing the symmetry stabilises $E_S^{n/f}$ and turns E_A^s into an edge state by removing the unstable direction associated with R_π-disrupting perturbations. A square root fit analogous to that of (6.1) to the few leftmost points on the E_A^s branch fixes the occurrence of P_{2S} at $Re_{P_{2S}} = 355.05 \pm 0.02$, very close to the value reported by Chen *et al.* (2013), and attests to the subcritical nature of the pitchfork bifurcation. The evolution of the leading eigenvalue of E_S across the critical point is also consistent with a pitchfork bifurcation. The eigenvalue is real and crosses the imaginary line, from positive to negative, while that of E_A^s starts from the origin of the complex plane and moves along the positive real axis away from the bifurcation point. Somewhere in between $Re = 365$ and 370, the leading eigenvalue of E_S, already in the stable half of the complex plane, collides with a subleading eigenvalue moving towards instability, and the couple merges and splits into a complex-conjugate pair in a non-bifurcation node-focus transition (see the evolution of λ_i in figure 11*b*). The count and stability of the solutions does not change, but the stable manifold of E_S is no longer governed by two distinct eigenmodes, but a complex pair that induces a spiralling recovery of the equilibrium. The real part of the leading complex pair of eigenvalues of E_S is seen to evolve in the direction of becoming unstable already in figure 11(*b*). Indeed, the pair crosses the imaginary axis as Re is increased further. Complex eigenvalues have been estimated from oscillatory exponential fits to the linear regime of the $v_\backslash$ time series (see Appendix B).

Figure 12(*a*) illustrates the analsysis of the Hopf bifurcation undergone by the focus E_S, which occurs somewhere in between $Re = 425$ and 500 (see figures 10*d* and 4). In this case, solutions are characterised by the oscillation amplitude $A_{u_\backslash} = u_\backslash^{max} - u_\backslash^{min}$ to detect time dependence. The symmetric equilibrium E_S has zero amplitude all along, but evolves

https://doi.org/10.1017/jfm.2026.11516 Published online by Cambridge University Press

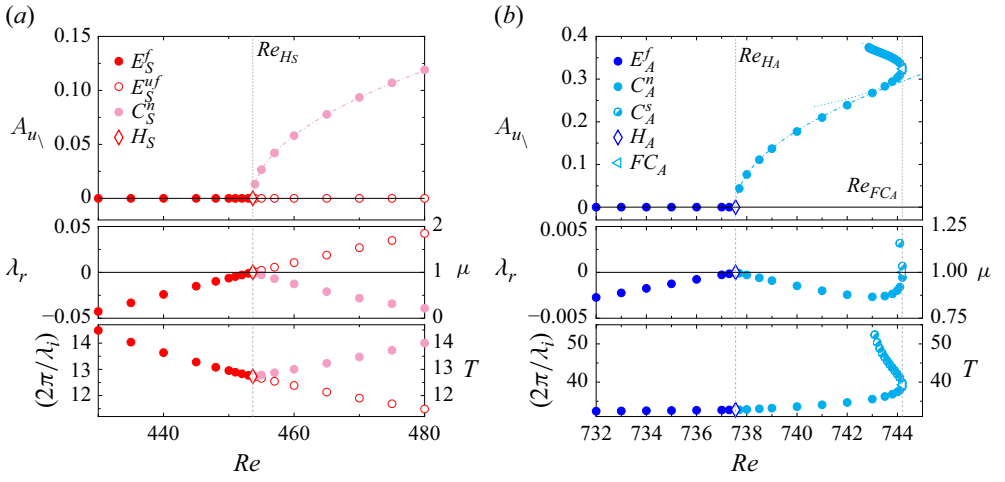


Figure 12. Hopf bifurcations of the steady states E_S and E_A and fold of cycles of C_A. (*a*) Supercritical Hopf bifurcation H_S of the base state E_S, breaking the $M_\backslash$ symmetry and producing the *ST* symmetric cycle C_S. (*b*) Supercritical Hopf bifurcation H_A of the steady state E_A, producing the cycle C_A, and fold bifurcation FC_A of the latter. The oscillation amplitude $A_{u_\backslash} = u_\backslash^{max} - u_\backslash^{min}$ (nil for steady states), the bifurcating eigenvalue $\lambda = \lambda_r + \mathrm{i}\lambda_i$ of the steady states, and the period T and multiplier μ of the bifurcated cycles are monitored as a function of Re. Dash-dotted and dotted lines denote square root fits to pinpoint Hopf and cyclic fold bifurcations, respectively.

from stable to unstable across the Hopf bifurcation. Meanwhile, the *ST* symmetric cycle C_S starts with zero amplitude that grows with increasing Re. A square root fit following

$$A_{u_\backslash}^{fit} = A_{u_\backslash}^{1}\sqrt{Re - Re_{H_S}} \tag{6.2}$$

to the few points closest to the critical point, establishes the occurrence of a supercritical Hopf bifurcation at $Re_{H_S} = 453.6766 \pm 0.0004$. This value is very close to the 452.8 reported by Meseguer *et al.* (2024), despite their smooth (or rather only moderately sharp) regularisation of corner singularities. The real part of the leading eigenpair of E_S crosses the imaginary axis at precisely this point and the dominant multiplier of the bifurcated cycle C_S is real, starts on the unit circle ($\mu = 1$) and decreases thereafter. The bottom subpanel depicts the quantity $2\pi/\lambda_i$ for the leading eigenpair of E_S instead of the imaginary part λ_i to allow comparison with the period T of C_S. As expected, the period of the cycle is inherited from the angular frequency associated with the bifurcating eigenpair of the steady state at the bifurcation point, but evolves independently away from it. See Appendix B for a detailed account of the stability analysis of periodic solutions.

Because of its involving a global bifurcation, we shall postpone the discussion on the fate of C_S to the next section and deal instead now with the remaining local bifurcations that befall the stable E_A branch and its offshoots. Recall that $E_A^n \to E_A^f$ has already transitioned from node to focus half-way between P_{1S} and $Re = 300$ (see figure 10*b*). Nothing much happens along the branch across a wide Reynolds number range until some place in between $Re = 732$ and 740 (see figures 10*f* and 10*g*), where the focus becomes unstable and a R_π-invariant but $M_\backslash$-asymmetric limit cycle materialises. If there are two branches of E_A^f mutually related by the $M_\backslash$ symmetry, the same holds for C_A and the Hopf bifurcation H_A at its origin. The analysis of H_A is shown in figure 12(*b*). A fit like that of (6.2) to the leftmost amplitudes of the converged C_A cycles sets the supercritical Hopf bifurcation at $Re_{H_A} = 737.554 \pm 0.002$. In this case, the comparison with the regularised 4LDSSC

https://doi.org/10.1017/jfm.2026.11516 Published online by Cambridge University Press

flow is not so favourable (see Meseguer *et al.* 2024, where a value of 698.4 was reported), but this was expected, since their Re_{SN_A} was also off with respect to the non-regularised problem (Chen *et al.* 2013). The evolution of the real and imaginary parts of the leading eigenpair is again consistent with the occurrence of a Hopf bifurcation, and the same can be said about the period and the dominant multiplier of the bifurcated cycle. Unlike what happened for H_S, where we had access to all solutions involved in the bifurcation, for H_A, we have to do without the unstable focus E_A^{uf} into which the steady state evolves. Having a 2-D unstable manifold that can neither be stabilised by symmetry enforcement nor by edge tracking places it beyond reach of time evolution. Its depiction in phase maps beyond Re_{H_A} has been approximated with a quadratic extrapolation from the latest available stable instances at $Re = 737$, 738 and 739.

This same figure 12(*b*) contains the necessary elements for a rough analysis of the fold-of-cycles to which the limit cycle branch C_A is subject at slightly higher values of the parameter, between $Re = 744$ and 800 (see figures 7 and 10*h*). Since the C_A branch had not been reported in the literature, neither had the eventual occurrence of a fold-of-cycles. Two closeby versions of the cycle, one stable (C_A^n) and the other unstable (the saddle C_A^s), coexist at the lower Re but have disappeared at the higher. The unstable cycle C_A^s can be converged to reasonable accuracy by deploying edge tracking between some velocity field on the stable cycle C_A^n and either the symmetric equilibrium E_S^{uf} or another velocity field on the stable ST-symmetric cycle $C_{S'}$, and bisecting between the last trajectory falling back on C_A^n and the first to leave towards $C_{S'}$. Be as it might, the amplitudes of C_A^n and C_A^s approach each other as Re is increased towards a critical point. A square root fit following

$$A_{u_\backslash}^{fit} = A_{u_\backslash}^0 + A_{u_\backslash}^1 \sqrt{Re_{FC_A} - Re} \tag{6.3}$$

to the rightmost points on the stable focus branch, this time allowing for a vertical shift $A_{u_\backslash}^0$, provides an estimate for the cyclic fold as taking place at $Re_{FC_A} = 744.193 \pm 0.002$. A parabolic fit of the form $Re^{fit} = Re_{FC_A} - ((A_{u_\backslash} - A_\backslash^0)/A_\backslash^1)^2$ using points on both the stable and unstable sides of the branch would have served the same purpose. The dominant multiplier μ is real throughout, but exits the unit circle precisely as the branch bends back in the fold of cycles. The period T also evolves continuously across the bifurcation and its rapid increase as Re is lowered along the saddle branch is an indicator that a boundary crisis is close at hand. In a boundary crisis, a time dependent solution (usually a strange attractor; periodic orbits in our case) comes into contact with a saddle solution (always E_A^s for the 4LDSSC flow) and/or with its stable manifold and disappears catastrophically. As a result, the phase space topology is reconfigured and phase space regions are reconnected differently, meaning that initial conditions that evolved into one attractor may lead to another after the crisis. We will investigate the crisis of C_A^s, along with two others involving the other two limit cycles, in the next section.

The full set of local bifurcations of the R_π-invariant 4LDSSC problem in the studied range $Re \in [0, 1000]$ is completed by a saddle-node point at which the nodal and saddle branches of E_A collide and disappear. This has been reported to happen at $Re \simeq 876.6$ for the singular corners cavity (Chen *et al.* 2013) and at $Re \simeq 708.4$ for the regularised cavity (Meseguer *et al.* 2024). Our time-stepping approach loses track of the nodal branch E_A^{uf} beyond the Hopf bifurcation H_A and the accuracy of the saddle branch E_A^s, although in principle accessible through edge tracking, is compromised by the divergingly slow dynamics that are typical of a saddle-node point. Consequently, it has not been possible to study this final bifurcation in any detail, other than by noting the disappearance of E_A^s,

https://doi.org/10.1017/jfm.2026.11516 Published online by Cambridge University Press

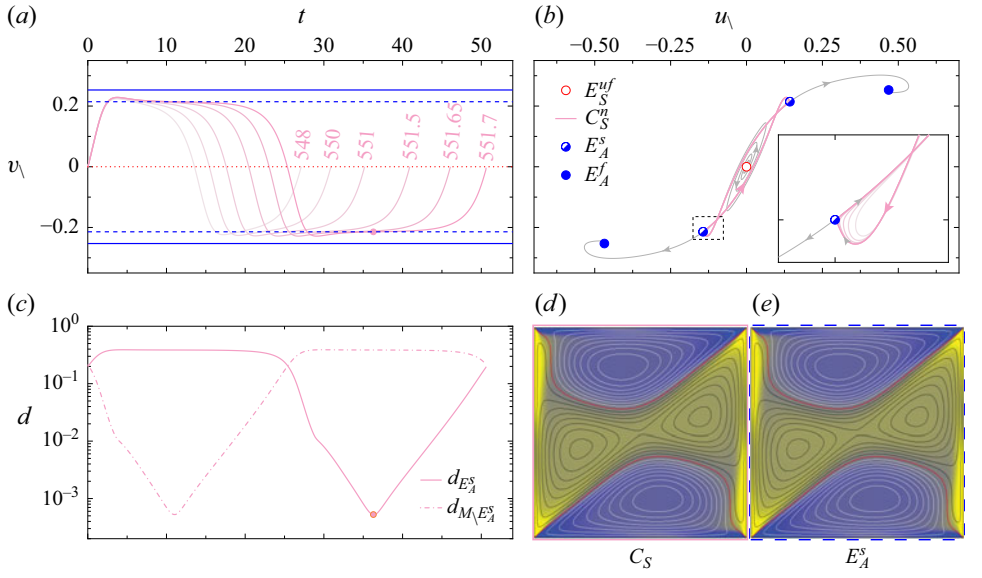


Figure 13. Heteroclinic bifurcation of C_S. (*a*) Time series $v_\backslash(t)$ of several C_S (pink solid lines with labels indicating *Re*) approaching the bifurcation. The steady states E_S (dotted red), E_A^f (solid blue) and E_A^s (dashed blue) are indicated with horizontal lines. (*b*) Phase portrait at $Re = 551.7$, very close to the crisis at $Re_{Het_S} \simeq 551.73$. Styles as for figure 4. The inset shows a magnification around E_A^s. (*c*) Distances time series of C_S with respect to E_A^s ($d_{E_A^s}$, solid) and $M_\backslash E_A^s$ ($d_{M_\backslash E_A^s}$, dash-dotted) at $Re = 551.7$. The time axis is shared with panel (*a*). (*d*) Snapshot of C_S at the closest approach to E_A^s at $Re = 551.7$, indicated with pink bullets in the time series of panels (*a*) and (*c*). (*e*) The E_A^s state at the same *Re*.

as illustrated by the phase portraits at $Re = 800$ and $Re = 1000$ of figures 10(*h*) and 10(*i*), respectively.

6.2. *Global bifurcations*

We now turn our attention to the global bifurcations, none of which had been previously detected, let alone discussed in the literature, despite the fundamental part they play in the emergence of $C_{S'}$.

The *ST* symmetric limit cycle C_S created at H_S disappears at some point between $Re = 500$ and 600 (see figures 4 and 10*e*). The snapshot of figure 5(*d*) at $Re = 500$ is clearly suggestive of a close approach to the saddle steady-state E_A^s originated at P_{2S}, thus pointing at the possible occurrence of a boundary crisis in the form of a saddle-loop bifurcation. Such a crisis involves the collision of a limit cycle with a saddle steady solution, followed by its catastrophic disappearance. In the absence of symmetries, the limit cycle merges with the stable and unstable manifolds of the saddle state forming a non-robust homoclinic orbit. The symmetries of the 4LDSSC problem and of the solutions involved in the boundary crisis require that the collision occurs simultaneously and symmetrically with E_A^s and $M_\backslash E_A^s$, and that the manifolds connection is not homoclinic, i.e. from each of the saddles to itself, but heteroclinic, with the stable and unstable manifolds of both states connecting them back and forth in an heteroclinic loop. The analysis of the heteroclinic bifurcation Het_S of C_S is presented in figure 13. In particular, figure 13(*a*) shows a full period of the $v_\backslash(t)$ time series of several C_S at *Re* approaching the crisis (increasingly darker shades of pink, labels indicating *Re* value). As expected for a boundary crisis of a limit cycle, the period grows fast as the global bifurcation is approached, and the

https://doi.org/10.1017/jfm.2026.11516 Published online by Cambridge University Press

dynamics spend longer and longer times in the vicinity of the saddle state involved in the collision. The time spent in the neighbourhood of E^s_A and $M\backslash E^s_A$ (dashed blue horizontal lines), symmetrically in turns, is rapidly protracted as Re is increased. The approach, which could be a mere projection artefact is, to some extent, confirmed by the phase portrait of figure 13(*b*), particularly the inset, where C_S is seen to evolve increasingly closer to E^s_A, to the point of becoming confounded with one side of the stable and unstable manifolds of the saddle solution (grey lines with arrows) at $Re = 551.7$, very near the crisis. Definite confirmation of the approaching collision is provided by the distance time series $d_{E^s_A}$ (solid pink) and $d_{M\backslash E^s_A}$ (dash-dotted pink) of C_S with respect to E^s_A and $M\backslash E^s_A$, respectively, shown in figure 13(*c*). The encounter between cycle and saddles is seen to occur at very close quarters at $Re = 551.7$, and both the approach and departure follow the exponential behaviour that is characteristic of the linear regime of manifolds in the proximity of a saddle equilibrium. Indeed, the instantaneous flow field of C_S at the time that minimises the distance $d_{E^s_A}$ (figure 13*d* and supplementary movie 5) is indistinguishable from that of E^s_A (figure 13*e*) for all practical purposes.

The global bifurcation we are envisaging involves the simultaneous collision of a limit cycle with two hyperbolic saddle equilibria. For the collision of a stable limit cycle with a single hyperbolic saddle equilibrium (the homoclinic or saddle-loop bifurcation), the period of the former is known to diverge following a logarithmic law of the form

$$T \sim -\frac{1}{\lambda} \log |\alpha_c - \alpha|, \tag{6.4}$$

where α is the parameter (Re in our case), α_c is its value at the bifurcation point and $\lambda > 0$ is the eigenvalue of the saddle in the direction of its unstable manifold, which, together with the stable manifold merge to form a non-robust homoclinic orbit (Gaspard 1990). If the cycle is unstable, λ is the negative of the least stable eigenvalue of the saddle equilibrium. Following the same arguments as Gaspard (1990), but for a stable space–time symmetric cycle colliding simultaneously with a pair of saddles related by the Z_2 symmetry of which the space-time symmetry is a remnant, simply modifies (6.4) to

$$T \sim -\frac{2}{\lambda} \log |\alpha_c - \alpha|, \tag{6.5}$$

with the unstable eigenvalue contributing twice to the slowing of the dynamics on account of the two saddles involved. The limit cycle, rather than becoming a non-robust homoclinic orbit, transforms instead into a pair of heteroclinic connections between the two mutually symmetric saddles. The protraction of the period as the bifurcation is approached, which is dictated by the unstable eigenvalue, occurs at two mutually symmetric stages of the cycle, such that the period diverges exactly twice as fast as for the ordinary saddle-loop in the absence of symmetry.

Figure 14(*a*) depicts the period T of C_S as a funtion of Re. The divergence of the period is evident and a fit of the form $T = -2\lambda^{-1} \log(Re_{Het_S} - Re) + T_1$, following (6.5), places the heteroclinic bifurcation Het_S at $Re_{Het_S} = 551.73366 \pm 0.00006$ with $\lambda = 0.3977 \pm 0.0004$, in fair agreement with the leading eigenvalue of the saddle E^s_A, which has been estimated as $\lambda_{E^s_A} = 0.39136 \pm 1 \times 10^{-5}$ at Re_{Het_S}.

At some place in bewteen the phase portraits at $Re = 600$ and 732 (figures 10*e* and 10*f*), the $C_{S'}$ periodic orbit comes to exist without the mediation of a Hopf or a cyclic fold bifurcation. Parametric continuation of the $C_{S'}$ branch in the direction of decreasing Re has the periodic orbit disappear slightly below $Re \lesssim 727$. The time series $v_\backslash(t)$ of $C_{S'}$, shown in figure 15(*a*) for decreasing values of Re, preserves the same temporal structure,

https://doi.org/10.1017/jfm.2026.11516 Published online by Cambridge University Press

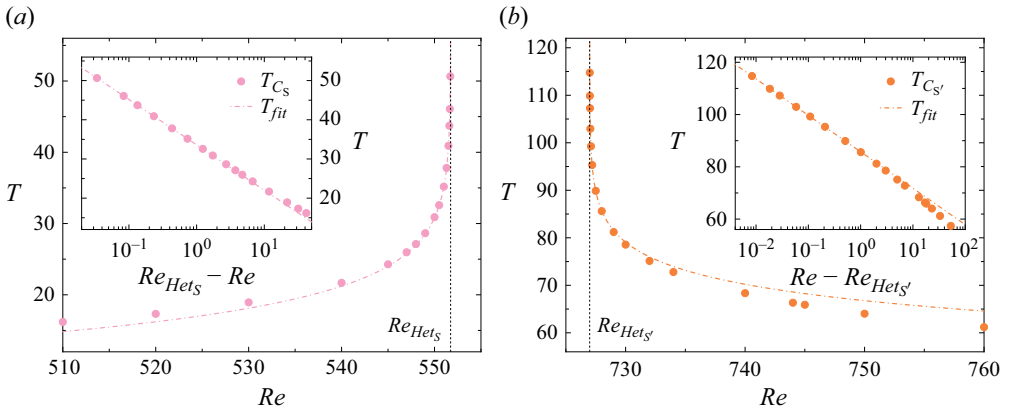


Figure 14. Heteroclinic bifurcations of the ST-symmetric limit cycles (*a*) C_S and (*b*) $C_{S'}$. Period T as a function of Re. The dash-dotted lines are logarithmic fits to a few data points closest to the crisis, indicated with the vertical asymptote. The inset presents the same data in log–log scale.

with alternated overshoot of E^f_A and $M_\backslash E^f_A$ (solid blue), followed each by increasingly protracted relaxation onto E^s_A and $M_\backslash E^s_A$ (dashed blue), respectively, that results in the overall elongation of the period. The phase portrait (figure 15*b*) reveals a close approach to E^s_A (see the inset) to the point that, at $Re = 727$, the cycle $C_{S'}$ becomes indistinguishable form the stable and unstable manifolds of the saddle (grey arrows). The flow field distance time series $d_{E^s_A}$ and $d_{M_\backslash E^s_A}$ of figure 15(*c*) confirm that the visits of the cycle to the saddles are indeed legitimate and not an artefact of the phase map projection. The similarity of the flow field colourmaps of $C_{S'}$ at the closest approach to E^s_A (figure 15*d*, and supplementary movie 6) and of the saddle itself (figure 15*e*) attest to the proximity of a boundary crisis. Thorough examinination of the divergence of the period T as a function of Re, as done in figure 14(*b*), and a logarithmic fit following $T = -2\lambda^{-1}\log(Re - Re_{Het_{S'}}) + T_1$, pinpoints the occurrence of the heteroclinic bifurcation $Het_{S'}$ at $Re_{Het_{S'}} = 726.9916 \pm 0.0004$ with $\lambda = 0.330 \pm 0.004$, in excellent agreement with the leading eigenvalue $\lambda_{E^s_A} = 0.33110 \pm 3 \times 10^{-5}$ of E^s_A at the bifurcation.

The phase portrait at $Re = 744$ (figure 7) features an unstable asymmetric limit cycle C^s_A that was not present at $Re = 740$ (figure 10*g*). We have already shown that this cycle results from a cyclic fold with the stable nodal cycle C^n_A at the slightly higher Re_{FC_A}, the analysis of which was presented in figure 12(*b*). This same figure holds the key for interpreting the fate of C^s_A as the parameter is lowered from the fold of cycles. The branch of saddle cycles has larger amplitude than the nodal branch and increases away from the fold, as also does the period, which seems to eventually diverge. This is a manifest sign that an infinite period bifurcation may be in play.

Figure 16 clarifies the situation and reveals the advent of a homoclinic bifurcation. For completeness, we have included in the figure solutions across both the Hopf (H_A) and cyclic fold (FC_A) bifurcations. Figure 16(*b*) essentially depicts the phase portrait at the homoclinic bifurcation point (Re_{Hom_A}), but includes also the stable equilibrium E^f_A (circles of increasingly darker blue) from $Re = 550$ in steps $\Delta Re = 50$ up to H_A (blue empty circle) and the stable nodal cycle C^n_A at several Re from H_A to the FC_A (lines transitioning from blue to cyan up to Hom_A, followed by increasingly lighter shades of cyan thereafter). The four C^n_A cycles in the range Re_{Hom_A} to Re_{FC_A} ($Re = 743$, 743.5, 744 and 744.2) are in one to one correspondence with coexisting saddle cycles C^s_A, drawn in the same shade but with dashed lines. The C^n_A grows fast after its appearance in the Hopf bifurcation, then the

https://doi.org/10.1017/jfm.2026.11516 Published online by Cambridge University Press

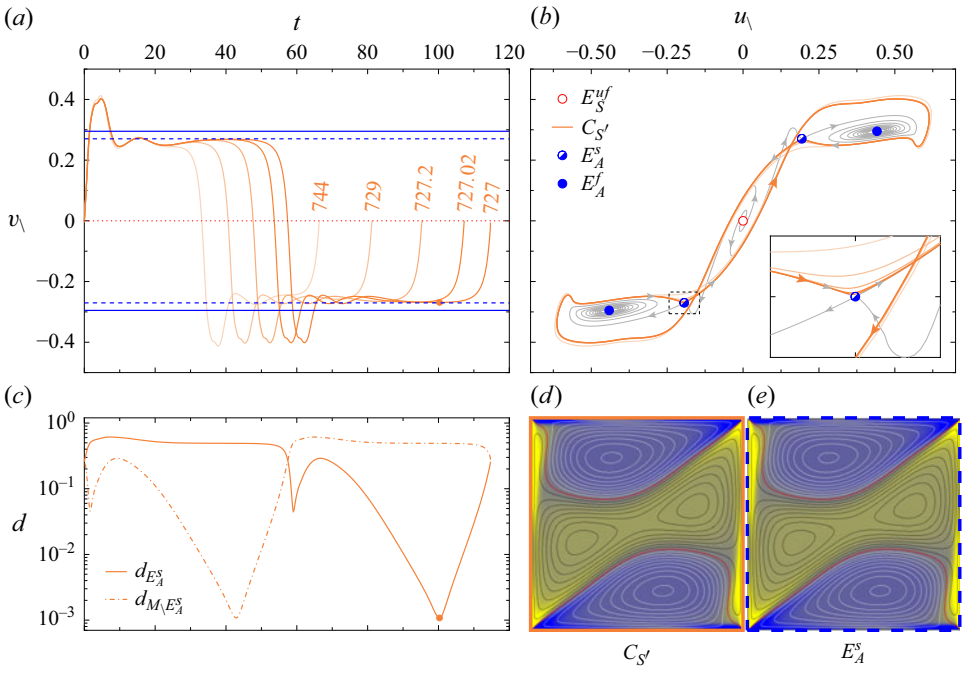


Figure 15. Heteroclinic bifurcation of $C_{S'}$. (*a*) Time series $v_\backslash(t)$ of several $C_{S'}$ (orange solid lines with labels indicating *Re*) approaching the bifurcation. The steady states E_S (dotted red), E^f_A (solid blue) and E^s_A (dashed blue) are indicated with horizontal lines. (*b*) Phase portrait at $Re = 727$, very close to the crisis at $Re_{Het_{S'}} \simeq 726.99$. Styles as for figure 7. The inset shows a magnification around E^s_A. (*c*) Distances time series of C'_S with respect to E^s_A ($d_{E^s_A}$, solid) and $M_\backslash E^s_A$ ($d_{M_\backslash E^s_A}$, dash-dotted) at $Re = 727$. The time axis is shared with panel (*a*). (*d*) Snapshot of $C_{S'}$ at the closest approach to E^s_A at $Re = 727$, indicated with orange bullets in the time series of panels (*a*) and (*c*). (*e*) The E^s_A state at the same *Re*.

growth rate relaxes for a while before speeding up again as the fold is approached. The larger C^n_A and the smaller C^s_A, corresponding to the same $Re = 744.2$, are already on the verge of colliding and disappearing in the cyclic fold at Re_{FC_A}. From the fold backwards, but now on the saddle branch, the C^s_A keep growing and conspicuously approach the saddle equilibrium E^s_A.

The $v_\backslash$ time series of figure 16(*a*), drawn in the same colours and shadings as figure 16(*b*), illustrate the full evolution of C_A along its branch. The nodal cycle C^n_A starts with vanishing amplitude, nearly sinusoidal time dependence and short yet finite period following H_A. The amplitude increases fast thereafter and the period slowly, and both keep increasing up to FC_A. The cycle becomes unstable at the fold and the branch bends back towards lower *Re*, now transformed into the saddle C^s_A. As *Re* is decreased towards the crisis, the amplitude keeps growing, albeit slowly, while the period increases fast as the dynamics spend increasingly longer times in the vicinity of E^s_A (horizontal blue dashed line). Definite evidence that the slowing dynamics are associated with a forthcoming collision with E^s_A is provided by figure 16(*c*), where the instantaneous distance $d_{E^s_A}$ from C^s_A to E^s_A is shown to decrease exponentially fast as the saddle equilibrium is approached and then depart again exponentially fast shadowing its unstable manifold at $Re = 742.87$, close to the bifurcation. To fathom the proximity of the fly-by, figures 16(*d*) and 16(*e*) (and supplementary movie 7) compare flow fields of C^s_A and E^s_A, respectively, at the time instant

https://doi.org/10.1017/jfm.2026.11516 Published online by Cambridge University Press

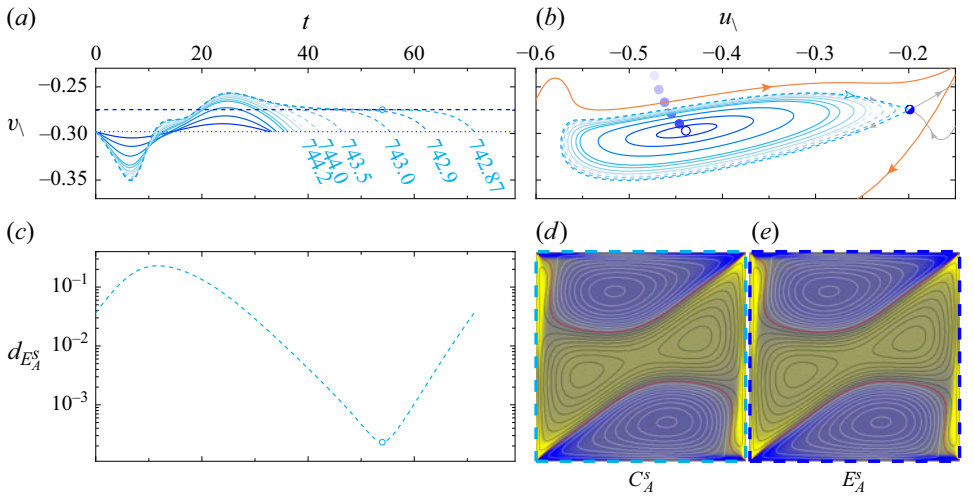


Figure 16. Homoclinic bifurcation C^s_A. (*a*) Time series $v_\backslash(t)$ of several C_A (solid blue-to-cyan lines for the nodal cycle C^n_A and dashed cyan with labels indicating Re for the saddle cycle C^s_A; same colour denotes same Re) approaching the bifurcation. The steady states E^{uf}_A (dotted blue, extrapolated) and E^s_A (dashed blue) are indicated with horizontal lines. (*b*) Phase portrait at $Re = 742.87$ accompanied by solutions on the asymmetric branch at several other Re leading to the bifurcation. The steady state E^f_A is shown from $Re = 550$ on in steps $\Delta Re = 50$ (filled circles of increasingly darker shades of blue) up to the Hopf point (empty blue circle). The nodal cycle C^n_A is depicted at $Re = 737.7$, 739 and 741 (solid lines transitioning from blue to cyan) up to the homoclinic bifurcation and at several Re beyond (increasingly light shades of cyan up to the cyclic fold at Re_{FC_A}). The saddle cycle C^s_A is shown at the same Re as the C^n_A (increasingly dark shades of cyan from the cyclic fold to the homoclinic point, with labels indicating Re). (*c*) Distance $d_{E^s_A}$ time series of C^s_A with respect to E^s_A at $Re = 742.87$. The time axis is shared with panel (*a*). (*d*) Snapshot of C^s_A at the closest approach to E^s_A at $Re = 742.87$, indicated with cyan bullets in the time series of panels (*a*) and (*c*). (*e*) The E^s_A at the same Re.

corresponding to the closest approach of the cycle to the saddle equilibrium, indicated with cyan bullets in figures 16(*a*) and 16(*c*). As expected, there is no telling them apart.

Unlike the heteroclinic bifurcations Het_S and $Het_{S'}$, which involved ST-symmetric cycles and mutually symmetric saddle equilibria, the boundary crisis we have now at hand concerns only an asymmetric cycle and a single equilibrium. The symmetries of the LDSSCF problem imply that all solutions breaking the $M_\backslash$ symmetry must occur in pairs and the same applies to all bifurcations undergone by these solutions. The boundary crisis of C^s_A upon hitting E^s_A is not an exception, so that $M_\backslash C^s_A$ must be colliding with $M_\backslash E^s_A$ at the same exact Re. Since E^s_A is an hyperbolic saddle equilibrium, the boundary crisis is a homoclinic (or saddle-loop) bifurcation, whereby the cycle and the stable and unstable manifolds of the equilibrium merge in a non-robust homoclinic orbit connecting instantly the equilibirum with itself and the periodic orbit disappears thereafter. In this type of infinite period bifurcation, the period T is known to diverge following (6.4), so figure 17 explores the evolution of T as a function of Re. A logarithmic fit according to $T = -\lambda^{-1}\log(Re - Re_{Hom_A}) + T_1$, locates the homoclinic bifurcation Hom_A as occurring at $Re_{Hom_A} = 742.8643 \pm 0.0002$ with $\lambda = 0.187 \pm 0.004$. The C^s_A being a saddle cycle, the fitting parameter λ is to be compared with the stable, rather than the unstable, eigenvalue of the saddle equilibrium. The least stable of the stable eigenvalues of E^s_A at Re_{Hom_A} has been estimated, from exponential fits to the final stages of the edge tracking trajectories leading to the saddle equilibrium, as $\lambda_{E^s_A} = -0.195 \pm 0.008$, which is compatible with the divergence rate of the period of C^s_A.

https://doi.org/10.1017/jfm.2026.11516 Published online by Cambridge University Press

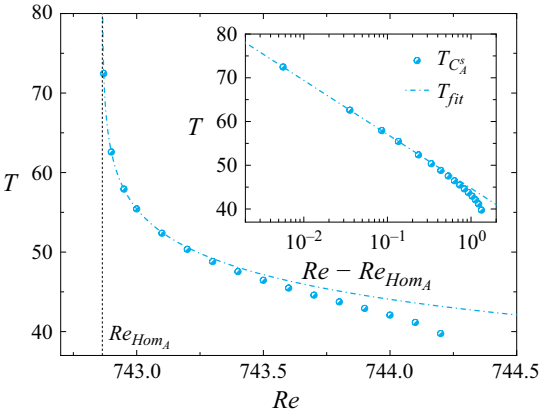


Figure 17. Homoclinic bifurcation of C_A. Period T as a function of Re. The dash-dotted line is a logarithmic fit to a few data points closest to the crisis, indicated with the vertical asymptote. The inset presents the same data in log–log scale.

7. Double-zero bifurcation with Z_2 symmetry and degeneration of third-order coefficients

We will now argue that the solutions, bifurcations and phase space topologies reported in the preceding sections are compatible with a 1-D parameter sweep in the vicinity of a codimension-4 point. The one-dimensionality of our exploration does not allow for the direct determination of the change of variables that would transform the 4LDSSC flow problem into the corresponding normal form, which would not be of any particular use anyway. Instead, we will draw the correspondence from phenomenological observation.

The double zero bifurcation with Z_2 symmetry was first studied by Takens (1974) as an approximating ordinary differential equations system to the 1 : 2 strong resonance in the context of codimension-2 bifurcations of maps. Provided non-degeneracy of the third order terms is granted, a complete unfolding of the normal form is given by

$$\left\{\begin{array}{l} \dot{x} = y, \\ \dot{y} = \alpha x + \beta y + s x^3 - x^2 y, \end{array}\right. \tag{7.1}$$

with $s = \pm 1$, of which only $s = -1$ is structurally stable. The associated bifurcation diagrams feature states akin to E_S, E_A, C_S, C_A and $C_{S'}$, but lack several of the characteristic features observed in the 4LDSSC problem. Knobloch (1986) presented the normal forms for the double zero bifurcation subject to failure of the non-degeneracy conditions, both for the cases with and without reflectional symmetry. In the case of mirror symmetry, up to four nonlinear terms of up to fifth order need be retained. If the degeneracy affects the two extant third-order terms (Knobloch 1986, case 4B), a complete unfolding of the structurally stable normal form of the reflectionally symmetric double zero bifurcation is given by

$$\left\{\begin{array}{l} \dot{x} = y, \\ \dot{y} = \alpha x + \beta y + \gamma x^3 + \delta x^2 y - x^5 - x^4 y, \end{array}\right. \tag{7.2}$$

and the full collection of bifurcation diagrams was produced by Dangelmayr *et al.* (1986), henceforth abreviatted as D86. Notice that we have reversed the sign of all four parameters (α, β, γ, δ) with respect to D86 for consistency with Knobloch (1986). These bifurcation diagrams contain almost all the phenomenology we have observed in the

https://doi.org/10.1017/jfm.2026.11516 Published online by Cambridge University Press

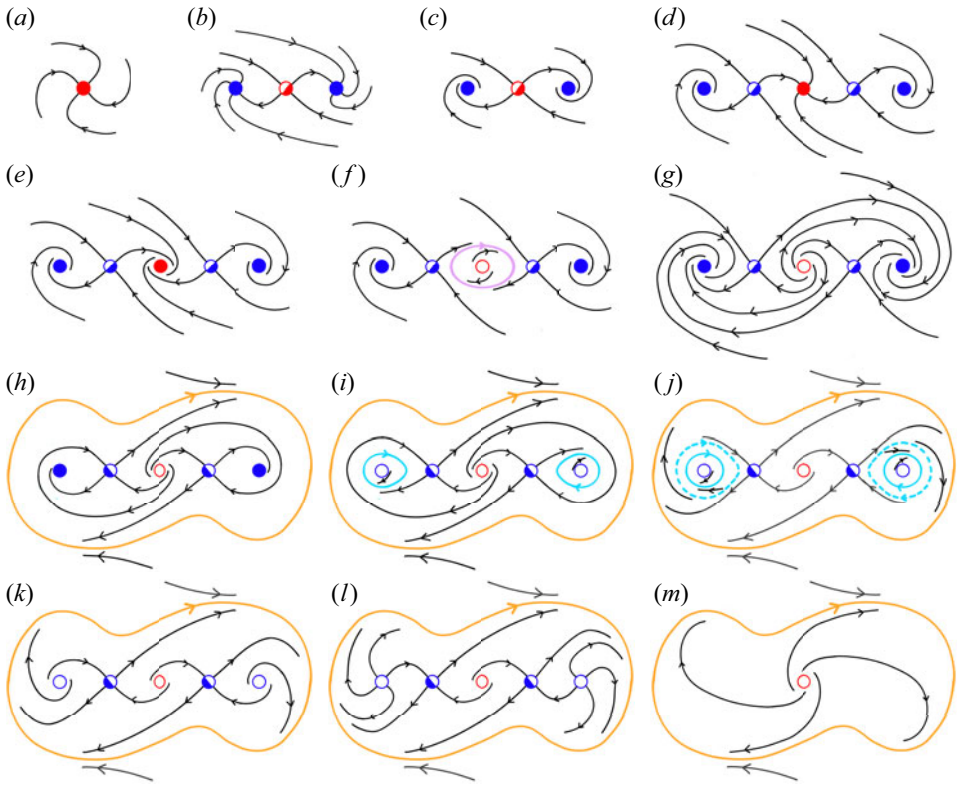


Figure 18. Structurally stable phase portrait sketches of the double zero bifurcation with Z_2 symmetry and degeneracy of the cubic terms that are relevant to the 4LDSSC flow problem.

4LDSSC flow problem. Our sweep in terms of Re can be interpreted as a 1-D path through the four-dimensional parameter space $(\alpha, \beta, \gamma, \delta)$. In particular, we start with $\alpha, \beta, \gamma, \delta < 0$ in region J1 of parameter space (see figures 2 and 3J in D86) and, in particular, with sketch 5.1, to be compared with our figure 10(a). To ease comparison with D86, we reproduce in figure 18 the phase portrait sketches that are relevant to the 4LDSSC problem, adapting colours and styles. Thus, figure 18(a) is a schematic representation of the case shown in figure 10(a) and corresponds to sketch 5.1 in D86. This and all correspondences discussed hereafter between the sketches in figure 18 and the phase portraits shown in previous sections or the sketches in D86 have been tabulated in table 2, to assist the reader. When Re is increased from its starting value, eventually α becomes positive, a pitchfork bifurcation occurs (P in D86, P_{1S} here), and the path crosses into region J5; compare sketch 5.5 of D86 with our figure 18(b), corresponding to figure 10(b), or, strictly speaking, figure 18(c). The difference between figures 18(b) and 18(c) illustrates a node-focus (NF_{1A}) transition of E_A. At this point, γ becomes positive and J5 turns into A5 with no intervening bifurcation (see figures 2 and 3A in D86). With γ already positive, α becomes negative again, the system undergoes a second pitchfork bifurcation (again P in D86, our P_{2S}), and the path crosses into region A16; see sketch 5.16 in D86 and our figures 18(d) and 18(e), corresponding to figures 10(c) and 10(d), respectively, which illustrate, incidentally, the node-focus transition of E_S. From there, β becomes positive, the system undergoes a Hopf bifurcation (H_0 in D86, H_S here) and the system lands in region A18 (sketch 5.18 in D86 versus figure 18f here, corresponding to figure 4). The path then traverses a heteroclinic bifurcation (SL_i in figure 6 of D86, Het_S of figure 13 here) into

https://doi.org/10.1017/jfm.2026.11516 Published online by Cambridge University Press

Phase portrait				Bifurcation/transition that follows						
Sketch (Figure)	4LDSSC (Figure)	D86	D85	Bif (here)	Sketch (Figure)	4LDSSC (Figure)	Bif (D86)	D86	Bif (D85)	D85
18(*a*)	10(*a*)	5.1	2.1	P_{1S}	—	—	P	—	P	—
18(*b*)	—	—	—	NF_{1A}	—	—	—	—	—	—
18(*c*)	10(*b*)	5.5	2.6	P_{2S}	—	—	P	—	P	—
18(*d*)	10(*c*)	—	—	NF_S	—	—	—	—	—	—
18(*e*)	10(*d*)	5.16	2.7	H_S	—	—	H_0	—	—	—
18(*f*)	4	5.18	2.8	Het_S	19(*a*)	13	SL_i	6.SL$_i$	SL_i	3.SL$_i$
18(*g*)	10(*e*)	5.17	2.9	$Het_{S'}$	19(*b*)	15	SL_+	6.SL$_+$	SL_a	3.SL$_a$
18(*h*)	10(*f*)	5.20	2.10	H_A	—	—	SL_a	6.SL$_a$	SL_b	3.SL$_b$
18(*i*)	10(*g*)	5.22	2.12	Hom_A	19(*c*)	16	H_a	—	H_a	—
18(*j*)	7			FC_A	20(*a*)	—				
18(*k*)	10(*h*)	5.19	2.13	NF_{2A}	—	—	—	—	—	—
18(*l*)	—	—	—	SN_A	20(*b*)	—	SN_a	—	SN_a	—
18(*m*)	10(*i*)	5.2	2.2	...						

Table 2. Correspondence of phase portraits and intervening bifurcations with those for the double zero bifurcation with Z_2 symmetry and degeneracy of cubic terms. Each row corresponds to a structurally stable phase portrait (first four columns) and the bifurcation or transition (last seven columns) that leads to the next. For each phase portrait and bifurcation/transition, the columns indicate the figures correspondence between our sketches (Sketch) and the actual flow problem (4LDSSC), the sketch of Dangelmayr *et al.* (1986) (D86) and the sketch of Dangelmayr *et al.* (1985) (D85). The correspondence between our naming of the bifurcations/transitions and those in D86 and D85 is also given in the columns labelled as Bif. Note that the correspondence fails for figures 18(i)/10(g) and 18(j)/7 because H_A and Hom_A are reversed (see shaded cells). Phase portraits and bifurcations/transitions not shown are indicated with a hyphen (–).

region A17 (figure 5.17 in D86, figure 18*g* here, akin to figure 10*e*). Sketches of the three global bifurcations observed in the 4LDSSC problem are shown in figure 19, reproducing the relevant sketches of figure 6 in D86, but with colours and styles matching those we have used throughout. The Heteroclinic point Het_S of figure 13 is schematically represented as figure 19(*a*). A second heteroclinic bifurcation (SL_+ of figure 6 in D86, $Het_{S'}$ of figure 19*b* here, corresponding to figure 15) takes the system into region A20 (figure 5.20 in D86, figure 18*h*, akin to figure 10*f*). At this point occurs the only discrepancy we have observed between our scenario and the unfolding of the reflectionally symmetric double zero bifurcation. As we have seen, the ensuing sequence takes the 4LDSSC problem through the Hopf (H_A), homoclinic (Hom_A) and cyclic fold (FC_A) bifurcations, while the double zero bifurcation concatenates the homoclinic (SL_a) and Hopf (H_a) bifurcations in reverse order and dispenses with the cyclic fold. Presumably, this is the effect of higher order terms that induce a crossing of the SL_a and H_a bifurcation lines, rendering the Hopf subcritical at a Bautin (or degenerate Hopf) bifurcation, whence a cyclic fold bifurcation line is issued (Kuznetsov 2023). The unique pair of asymmetric limit cycles observed by D86 is unstable and appears in the homoclinic bifurcation SL_a the same way our unstable C_A^s appears in Hom_A (compare sketches 6 and 5.22 in D86 with figures 19*c* and 18*j* here, corresponding to figures 16 and 7). In contrast, our Hopf H_A is supercritical and precedes Hom_A, while their Hopf H_a is subcritical and must necessarily come after SL_a. To restore the equivalence between Hom_A and SL_a, the limit cycle resulting from H_A must turn unstable, and hence the presence of the cyclic fold FC_A. A sketch of FC_A is depicted in figure 20(*a*), where the non-hyperbolic C_A cycle has been styled as dash-dotted. In a way, our figures 18(*i*) and 18(*j*), which are schematic representations of figures 10(*g*) and 7, replace the sketch 5.22 in D86. Either subsequence of bifurcations, that of the degenerate mirror symmetric double zero bifurcation or the one we have found for the 4LDSSC flow problem, leads to the

https://doi.org/10.1017/jfm.2026.11516 Published online by Cambridge University Press

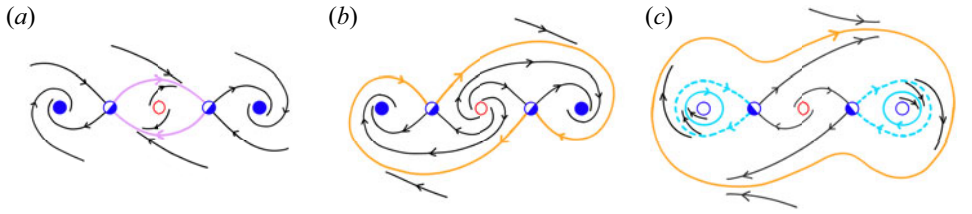


Figure 19. Phase portrait sketches of the global bifurcations occurring in the double zero bifurcation with Z_2 symmetry and degeneracy of the cubic terms that are relevant to the 4LDSSC flow problem.

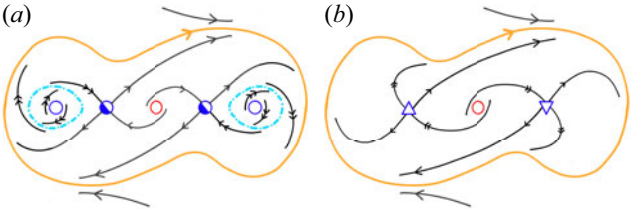


Figure 20. Phase portrait sketches of (*a*) the FC_A and (*b*) the SN_A bifurcations of the 4LDSSC flow problem. The non-hyperbolic C_A and E_A solutions are denoted with dash-dotted lines and triangles, respectively.

same state of affairs, region A19 (sketch 5.19 in D86 or figure 18*k* here, corresponding to figure 10*h*). The last step, and the only one we have not been able to study in any depth, takes the system across a saddle-node bifurcation (SN_A) into region A2 (sketch 5.2 in D86 and figure 18*m*, corresponding to figure 10*i*). For the occurrence of SN_A to be possible (see figure 20*b*, where the non-hyperbolic E_A is depicted with triangles), the focus E_A^{uf} must first become a node E_A^{un} in a reverse node–focus transition (NF_{2A}), as illustrated by the differences from figures 18(*k*) and 18(*l*).

In this parallel, the parameter δ remains negative all along. This suggests that the 4LDSSC problem may be understood in the framework of a codimension-3 bifurcation, rather than having to resort to the fully degenerate reflectionally symmetric double zero bifurcation, which is codimension-4. Actually, case 3B of Knobloch (1986), which has the degeneracy only in the term x^3, was unfolded by Dangelmayr *et al.* (1985) and already contains all the necessary ingredients. For reference, the parameter space regions 1, 5, 16, 18, 17, 20, 22, 19 and 2 of D86 correspond to 1, 6, 7, 8, 9, 10, 12, 13 and 2 of Dangelmayr *et al.* (1985), respectively.

Table 2 summarises, for completeness, the correspondence of phase portraits and intervening bifurcations of the 4LDSSC flow problem with those for the double zero bifurcation with Z_2 symmetry and degeneracy of cubic terms.

8. Concluding remarks

We have unfolded the full bifurcation diagram, up to a Reynolds number of $Re = 1000$, of the 2-D flow inside a square cavity, driven by the symmetric sliding of its four sides, all at equal velocity, and facing sides moving in opposite directions (4LDSSC), with the sole restriction of a rotational invariance of angle π about its centre (R_π). With this constraint, only one of the two remaining symmetries, either the mirror reflection with respect to one ($M_\backslash$) or the other ($M_/$) of the diagonals, plays a relevant role. A symmetric steady solution, E_S, exists all along. This base state is the only solution at sufficiently low *Re* and, as such, acts as a global attractor. At the other end of the *Re*-range studied, the base

https://doi.org/10.1017/jfm.2026.11516 Published online by Cambridge University Press

state, now unstable, is accompanied exclusively by a stable space–time symmetric limit cycle, $C_{S'}$, replacing it in the role of global attractor. The space–time symmetry, a vestige of the broken mirror symmetries, keeps the periodic orbit invariant to evolution over half a period, followed by reflection about either of the cavity diagonals. In the interim, another space–time symmetric limit cycle, C_S, a pair of asymmetric steady states, E_A, mutually related by either of the mirror symmetries, and a pair of asymmetric limit cycles, C_A, also mutually related by mirror symmetries, bifurcate and vanish in a complex succession of bifurcations, local and global. A sum total of nine bifurcations, two pitchfork (P_{1S}, P_{2S}), two Hopf (H_S, H_A), two heteroclinic (Het_S, $Het_{S'}$), one homoclinic (Hom_A), a cyclic fold (FC_A) and a saddle-node (SN_A), several actually occurring in mirror-symmetry-related pairs (those with the A subscript), mediate the transitions experienced by the phase space from the unicity of E_S at low Re to its coexistence with $C_{S'}$ at high Re. Although imposing the R_π invariance might appear, at first glance, to unrealistically overconstrain the problem, it is not so. The $C_{S'}$ cycle, whose origin is at the core of our analysis on account of its being the precursor to the onset of chaos, is stable in the full space, naturally preserving the R_π symmetry. Actually, the R_π-subspace is globally attracting, one or other of the R_π-invariant solutions acting as attractors in full space at all values of $Re < 1000$. Therefore, the R_π-restricted simulations must be merely understood as a resource to compute some of the unstable solutions which, although relevant to the genesis of $C_{S'}$, would have otherwise been inaccessible to time evolution.

Despite the abundance of bifurcations and the variety of intervening solutions, the full bifurcation scenario can be explained, with some minor adjustment, in terms of a 1-D path across the parameter space of a codimension-four bifurcation: the double zero bifurcation with Z_2 symmetry and degeneration of the cubic terms (Knobloch 1986). The sole adjustment concerns the nature of one of the Hopf bifurcations, H_A, which is supercritical for the 4LDSSC flow problem. To restore the diagrams of the degenerate symmetric double zero bifurcation (Dangelmayr *et al.* 1986), the 4LDSSC requires an additional cyclic fold, FC_A, the occurrence of which we have been able to ascertain. We surmise that, since the 4LDSSC problem is rather far from the codimension-four point, the full sequence of bifurcations spreading over several hundreds of Re, the higher-order terms could well have induced a Bautin bifurcation, this being the only alteration necessary to explain the discrepancy entirely. Actually, only one of the cubic terms needs be degenerate to account for the bifurcation diagram of the 4LDSSC problem, such that it can be regarded as a perturbation of a codimension-three point (Dangelmayr *et al.* 1985), rather than the full fledged codimension-four point. To explore in more detail the occurrence of the codimension-three bifurcation in the 4LDSSC problem, two additional parameters would be required for the unfolding. These parameters should, of course, preserve one of the mirror symmetries for the problem to retain the properties of the symmetric double zero bifurcation. An obvious choice is given by the partial disymmetrisation of the lid velocities, for example, setting $Re_T = Re_L \neq Re_R = Re_B$ to keep the $M_\backslash$ symmetry, while redefining $Re = \sqrt{Re_T^2 + Re_B^2 + Re_L^2 + Re_R^2}/2$. Here, $Re_X = U_X L/\nu$ is the Reynolds number based on the velocity of lid $X \in \{T, B, L, R\}$. The third parameter cannot incur any further disymmetrisation, so modifying lid velocities in any additional way is discarded. One option would be to modify the velocity distributions along the lids according to some regularisation parameter. Alternatively, morphing the square geometry into a rhombus could afford, in a more natural way, a third parameter that also preserves the mirror symmetries. Unfolding the codimension-three bifurcation is left for future consideration, as it indeed bears physical relevance. Aptly tuning the additional

https://doi.org/10.1017/jfm.2026.11516 Published online by Cambridge University Press

parameters should, in principle, allow the stabilisation or destabilisation of solutions at will, thus enabling effective flow control.

Although most of the solutions are linearly stable to perturbations breaking the R_π invariance, some others (notably E_S after the P_{2S}, the whole C_S branch and part of the E_A^s branch) require the explicit enforcement of the rotational symmetry. Computations in the full phase space (no symmetry restrictions) suggest that, although there is no stable solution breaking the R_π symmetry, existing saddle solutions (Meseguer *et al.* 2024) capture the dynamics away from the R_π-symmetry phase space in the neighbourhood of the R_π-unstable solutions and then reinject the trajectories back onto the R_π-symmetry phase space in the vicinity of the R_π-stable solutions. The analysis of this phenomenon has been left out of the scope of this paper, but may be worth considering.

Finally, it is not clear how much of the bifurcation diagram explored here for the 2-D 4LDSSC problem may persist in a 3-D set-up. We plan to undertake 3-D computations in spanwise extended cavities of varying aspect ratio, both with periodic and stationary no-slip wall boundary conditions in the near future to explore this.

Supplementary movies. Supplementary movies are available at https://doi.org/10.1017/jfm.2026.11516.

Acknowledgements. We are profoundly indebted to Eva López Rosa for her invaluable contribution in drawing the sketches of figures 18, 19 and 20. Fernando Mellibovsky is a Serra-Húnter fellow

Data availability statement. The data that support the findings of this study will be handed over upon reasonable request.

Funding. This research was supported by the Ministerio de Ciencia, Innovación y Universidades (Agencia Estatal de Investigación, project nos. PID2020-114043 GB-I00 (MCIN/AEI/10.13039/501100011033), PID2023-150029NB-I00 (MCIN/AEI/10.13039 /501100011033/FEDER, UE) and PID2023-150014OB-C21. Funding by the G2024 KY0613 project of Northwestern Polytechnical University and the 20230013053008 project by the Aeronautical Science Foundation of China are also aknowledged.

Declaration of interests. The authors report no conflict of interest.

Appendix A. Kinetic energy contours and wall shear stress distributions

This appendix is devoted to an extended discussion of the flow physics associated with the various solutions presented in the paper. The solutions are examined in the context of kinetic energy fields and skin friction coefficient distributions along the walls of the cavity. In the following, we use T, R, B and L to refer to the top, right, bottom and left walls, and TR, BR, BL and TL to denote the four corners.

The nondimensional kinetic energy fields are computed from the non-dimensional velocity fields according to

$$\kappa = \frac{1}{2}\boldsymbol{u}\cdot\boldsymbol{u} = \frac{u^2+v^2}{2}, \tag{A1}$$

while the skin friction coefficient results from the non-dimensionalisation of the wall shear stress τ_w following

$$C_f = \frac{2\tau_w}{\rho U^2} = \frac{2}{Re}\left(\boldsymbol{t}\cdot\frac{\partial \boldsymbol{u}}{\partial \boldsymbol{n}}\right)_w, \tag{A2}$$

where $\boldsymbol{t} = \boldsymbol{u}_w/\|\boldsymbol{u}_w\|$ is the wall tangent unit vector, $\partial/\partial\boldsymbol{n}$ is the directional derivative with respect to the exterior unit normal $\boldsymbol{n}$ and the w subscript denotes evaluation at the wall. Thus computed, positive C_f denotes shear opposing the sliding motion of the lid, thereby

https://doi.org/10.1017/jfm.2026.11516 Published online by Cambridge University Press

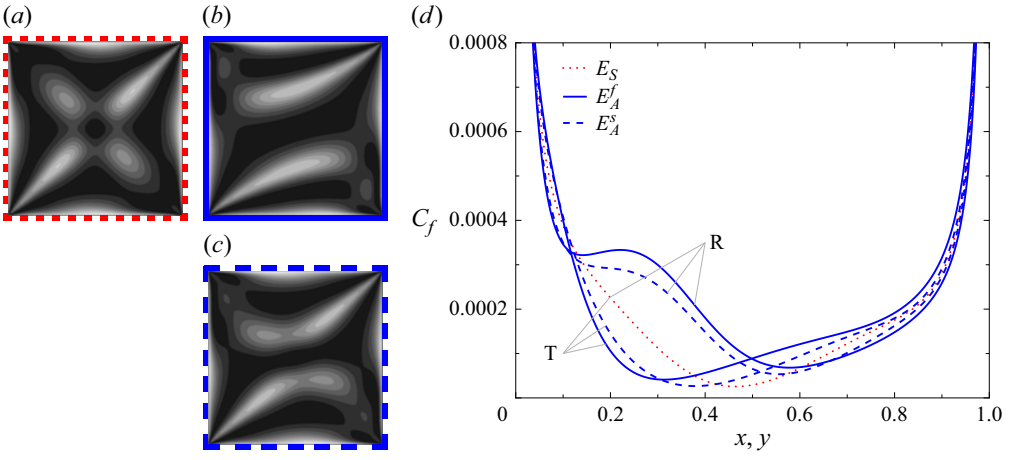


Figure 21. Steady states at $Re = 500$. Kinetic energy fields ($\kappa \in [0, 0.5]$, colourmap from black to white) of (*a*) E_S^{itf}, (*b*) E_A^f and (*c*) E_A^s. (*d*) Friction coefficient C_f along the top (T) and right (R) walls.

contributing to skin friction drag. In particular, we have, for the four walls,

$$C_f^{T,B}(x) = \frac{2}{Re}\left.\frac{\partial u}{\partial y}\right|_{y=\pm 0.5}, \quad C_f^{R,L}(y) = \frac{2}{Re}\left.\frac{\partial v}{\partial x}\right|_{x=\pm 0.5}. \tag{A3}$$

With these definitions, the R_π invariance entails $C_f^B(x) = C_f^T(-x)$, $C_f^L(y) = C_f^R(-y)$ and $\kappa(x, y) = \kappa(-x, -y)$, the $M_/$ symmetry has $C_f^T(x) = C_f^R(y)$, $C_f^B(x) = C_f^L(y)$ and $\kappa(x, y) = \kappa(y, x)$, and the $M_\backslash$ symmetry $C_f^L(y) = C_f^T(-x)$, $C_f^B(x) = C_f^R(-y)$ and $\kappa(x, y) = \kappa(-y, -x)$.

Figure 21 depicts κ fields and $C_f^{T,R}$ distributions for the three steady states at $Re = 500$. The κ field of E_S (figure 21*a*) preserves all three symmetries of the problem. The flow topology consists of two strong jets issued from the two corners where two of the lids run into each other (BL and TR), running along the diagonal and meeting head on at the centre of the cavity. The collision leaves a stagnant region in the centre of the cavity and forces each of the jets to split in two and rejoin in pairs along the TL-BR diagonal. The recombination results in two weaker jets which drive the fluid towards the TL and BR corner regions, whence the moving walls transport it back to the TR and BL corners. Thin layers of high-velocity fluid can also be identified in the immediate vicinity of each one of the sliding walls. In a reference frame moving at the sliding velocity of any given lid, the thin fluid region adjacent to it can be interpreted as an ordinary boundary layer. The C_f distributions along the T and R walls, shown in figure 21(*d*) (dotted red), are coincident on account of the $M_/$ symmetry. The friction diverges at the corners due to the discontinuity in the velocity and is lowest close to the midpoint along each of the walls, with the minimum slightly displaced towards the corner from which the lid is escaping. The weaker jets aimed towards the TL and BR corners compress the adjacent boundary layers, rendering them thinner and, consequently, increasing the friction on the upstream half of each one of the walls as compared with the downstream half. For E_A^f (figure 21*b*), the strong jets issued from the TR and BL corners avoid the collision by bending towards one of the contiguous walls, thus breaking both mirror symmetries. For the given instance of the solution pair, the TR jet leans towards the T lid, while the BL jet leans towards the B lid. For its symmetric counterpart, $M_/E_A^f = M_\backslash E_A^f$, the jets bend towards the L and R walls

https://doi.org/10.1017/jfm.2026.11516 Published online by Cambridge University Press

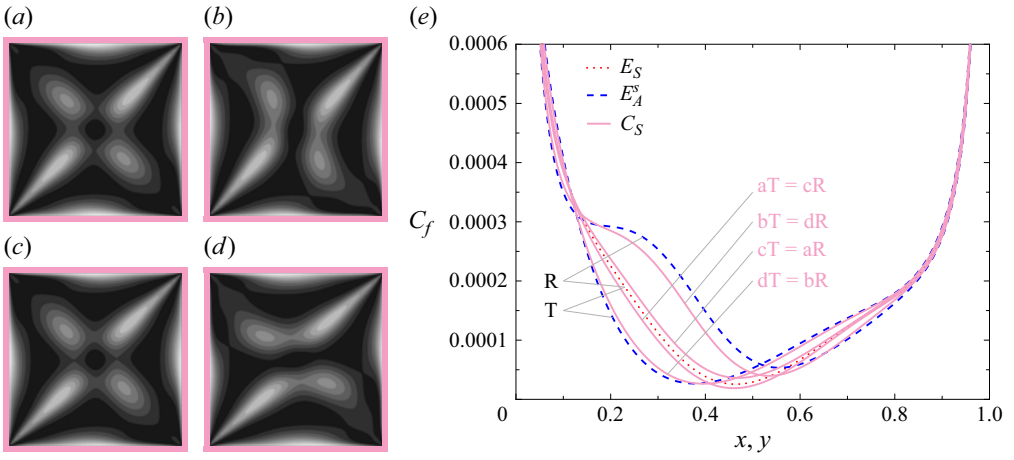


Figure 22. Space–time symmetric periodic orbit C_S at $Re = 500$. Kinetic energy κ snapshots at (*a*) t_0, (*b*) t_1, (*c*) t_2 and (*d*) t_3 (same instants as for figure 5). (*e*) Friction coefficient C_f along the top (T) and right (R) walls at the same time instants as the snapshots (see labels). The curves for E_S and E_A^s are shown for reference.

instead (not shown). The C_f distributions on the walls also break the mirror symmetries (figure 21*d*, solid blue). The minimum along the T wall moves further upstream towards the TL corner, while that along the R wall is somewhat shifted towards the TR corner and a region of noticeably increased shear arises in the upstream half of the wall. This increased shear is related to the strong jet issued from the BL corner, whose deviation towards the B wall has it impinge on the R wall, thereby compressing the boundary layer against it and thinning it accordingly. Meanwhile, the other strong jet impinges on the L wall and the weak jet that was pointed toward the TL corner, orignially fed by the jet collision at the cavity centre, is weakened if not altogether suppressed. As a result, the boundary layer on the upstream half of the T wall is no longer compressed and the friction in the region drops substantially. For E_A^s, the κ field is half-way between those for E_S and E_A^f, sharing the overall topology with the latter. The strong jets deviate from the BL-TR diagonal as for E_A^f, but the deviation is milder and vestiges of the weaker jets that were characteristic of E_S are still discernible along the TL-BR diagonal. The C_f distributions of E_A^s along the T and R walls break the mirror symmetry as for E_A^f but not as decidedly. As was the case with κ fields, C_f distributions of E_A^s remain half-way between those for E_S and E_A^f.

Still at $Re = 500$, four snapshots of the κ fields of C_S are shown in figure 22(*a–d*) at the same four time instants as in figure 5(*a–d*). The cyclic solution consists of a mild oscillation of the two strong jets about the TR-BL diagonal, alternately seeking collision and then avoiding it by bending towards opposite sides of the diagonal and each feeding one or the other of the weak jets driving fluid to the TL and BR corners. The four selected snapshots support the space–time symmetry ST of C_S and also the imperfect recovery of the mirror symmetries twice along the period. The flow oscillates between two extreme configurations that clearly break the mirror symmetries and approaches the E_A^s at t_3 (compare figures 22*d* and 21*c*) and its mirror-symmetric at t_1 (figure 22*b*), half a period apart. At instants t_0 and $t_2 = t_0 + T/2$, the κ fields are, if not fully mirror-symmetric, definitely mutually symmetric, and barely distinguishable from that for E_S (compare figures 22*a* and 22*c* with 21*a*). The C_f distributions of figure 22(*e*) further clarify the relation between C_S (pink lines with labels indicating lid – T or R – and time instant – a, b, c, d) and both E_S and E_A^s. The T and R walls have identical C_f distributions when

https://doi.org/10.1017/jfm.2026.11516 Published online by Cambridge University Press

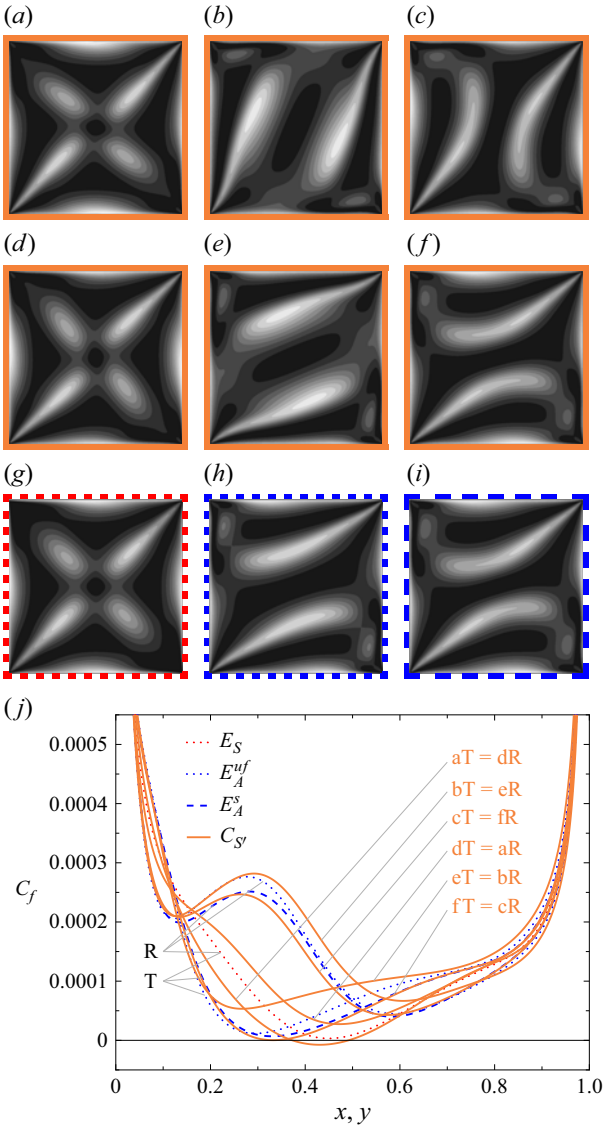


Figure 23. Space–time symmetric periodic orbit $C_{S'}$ at $Re = 744$. Kinetic energy κ snapshots at (*a*) t_0, (*b*) t_1, (*c*) t_2, (*d*) t_3, (*e*) t_4 and (*f*) t_5 (same instants as for figure 8). Also shown, for reference, are κ fields of (*g*) E_S, (*h*) E_A^{uf} and (*i*) E_A^s at the same $Re = 744$. (*e*) Friction coefficient C_f along the top (T) and right (R) walls at the same time instants as the snapshots (see labels). The curves for E_S, E_A^{uf} and E_A^s at $Re = 744$ are included for reference.

comparing time instants half a period apart, on account of the *ST* symmetry, and their evolution bounces back and forth between those for E_A^s (dashed blue) and $M_{\backslash} E_A^s$ (same dashed blue, but exchanging the R and T labels), closely approaching that for E_S (dotted red) twice every period.

The evolution of the flow topology of $C_{S'}$ bears some resemblance to that of C_S. Figure 23 shows κ fields and C_f distributions of $C_{S'}$ at $Re = 744$ at the same time instants as figure 8. The *ST* symmetry is evident when comparing κ fields half a period apart (figures 23*a* versus 23*d*, 23*b* versus 23*e* and 23*c* versus 23*f*), as also is the imperfect

https://doi.org/10.1017/jfm.2026.11516 Published online by Cambridge University Press

recovery of the mirror symmetries twice every period (figures 23*a* and 23*d*), although the misalignment of the jets is more obvious for $C_{S'}$ than for C_S. These are the instants (t_0, t_3) when $C_{S'}$ approaches E_S at closest quarters (see figure 23*g*). As for C_S, the dynamic evolution of $C_{S'}$ consists in the alternated oscillation of the strong jets about the TR-BL diagonal, but while for C_S the oscillation amplitude was bounded by the tilt angle of E_A^s, $C_{S'}$ has the jets explore larger tilt angles (figures 23*b*, *e* at times t_1 and t_4), amply exceeding those of E_A^{uf} (figure 23*h*, now an unstable focus). As the jet angle is restored from its maximum deviation towards the diagonal, the dynamics are temporarily slowed down at an intermediate angle (figures 23*c* and 23*f* at times t_2 and t_5) and the flow topology transiently approaches that of E_A^s (figure 23*i*) or its symmetric. The C_f distributions on the T and R wall for $C_{S'}$ are depicted in figure 23(*j*). The most remarkable difference with respect to the solutions at $Re = 500$ is that C_f cancels out and becomes negative, albeit only slightly, over a certain extent of the walls for some intervals along the full period of the oscillation, which is an indication that the boundary layer separates and then reattaches in what is commonly known as a recirculation or separation bubble. In particular, the T wall features a separation bubble at t_0 (aT, corresponding to snapshot figure 23*a*) and the R wall at $t_3 = t_0 + T/2$ (dR, snapshot figure 23*d*), when the flow is closest to E_S. For E_S however, the separation bubble is only incipient with a minimum $C_f \gtrsim 0$ simultaneously on all four walls.The missmatch between the formation of separation bubbles along a period of $C_{S'}$ and the presence of such bubbles in the steady states that are closest at any given time seems to be a dynamic effect. The separation bubbles at the times when $C_{S'}$ is closest to E_S (t_0, t_3) would seem to result from an overshooting induced by the rapid recovery of the jets towards symmetry after the temporary stagnation in the vicinity of E_A^s (t_5, t_2), which also features an incipient bubble on the walls towards which the jet leans. The solution E_A^{uf} is orbited around but never closely visited by $C_{S'}$. The separation bubbles were already visible, although not very conspicuously, in figures 8(*a*) and 8(*d*) as thin patches of positive (yellow) and negative (blue) vorticity adjoining the T and R walls, respectively. The dynamic evolution of the C_f distributions along a period of $C_{S'}$ shadow those corresponding to the coexisting steady states, particularly E_S and E_A^s, but unlike C_S, overshoots occur.

The evolution of the flow topology of the stable C_A^n (and of its symmetry related $M_\backslash C_A^n = M_/ C_A^n$) appears as a trimmed version of that of $C_{S'}$ that, instead of attempting resymmetrisation after visiting E_A^s and then falling onto the symmetry-conjugate region of phase space, opts instead for keeping the asymmetry. Four snapshots of the κ field along a full period of C_A^n at $Re = 744$ are shown in figure 24(*a–d*) at the same time instants as in figure 5(*a–d*). The strong jets now oscillate at either side of the diagonal, never crossing it, with average tilt angle about that of E_A^{uf} (see figure 23*h*), and bounded from below by that of E_A^f (see figure 23*i*), rather than from above, as was the case of C_S. At the closest visit to E_A^s (figure 24*d*, to be compared with figures 23*f* and 23*i*), the dynamics is transiently slowed down and, instead of having the jets accelerate towards head on collision and then cross the diagonal as for $C_{S'}$ (see figure 23*a*), they bounce back towards the closest wall (figure 24*a*). The C_A^n solution, with the tilt angle of the jet evolving between that of snapshots figures 24(*b*) and 24(*d*), seems to correspond to the $C_{S'}$ bouncing back and forth between snapshots figures 23(*e*) and 23(*f*). The $C_f^{T,R}$ distributions of C_A^n remain very similar at all times (figure 24*e*), evolving in a narrow band roughly bound from below by the distributions for E_A^s and oscillating about those for E_A^{uf}. Indeed, the distributions at t_3 of C_A^n are lowest and very close to those of E_A^s on both the T and R walls, but no separation

https://doi.org/10.1017/jfm.2026.11516 Published online by Cambridge University Press

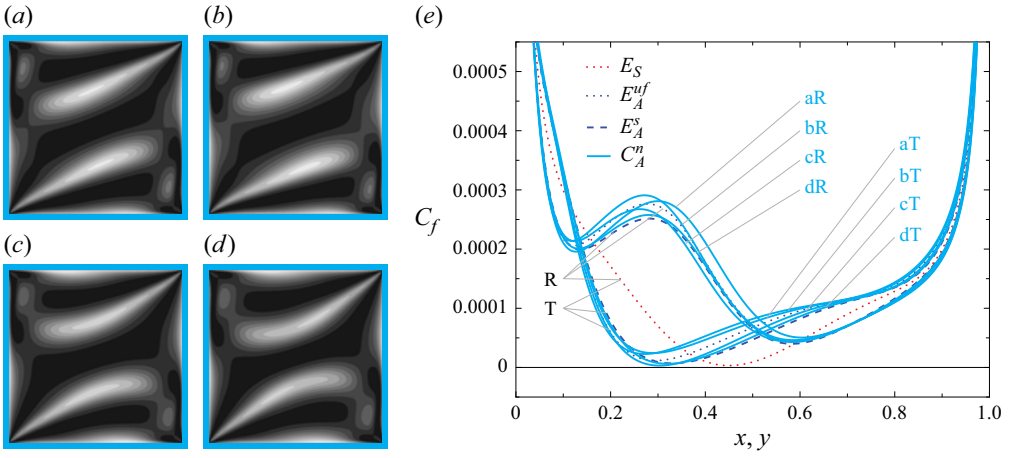


Figure 24. Non-mirror symmetric periodic orbit C_A^n at $Re = 744$. Kinetic energy κ snapshots at (*a*) t_0, (*b*) t_1, (*c*) t_2 and (*d*) t_3 (same instants as for figure 6). (*e*) Friction coefficient C_f along the top (T) and right (R) walls at the same time instants as the snapshots (see labels).

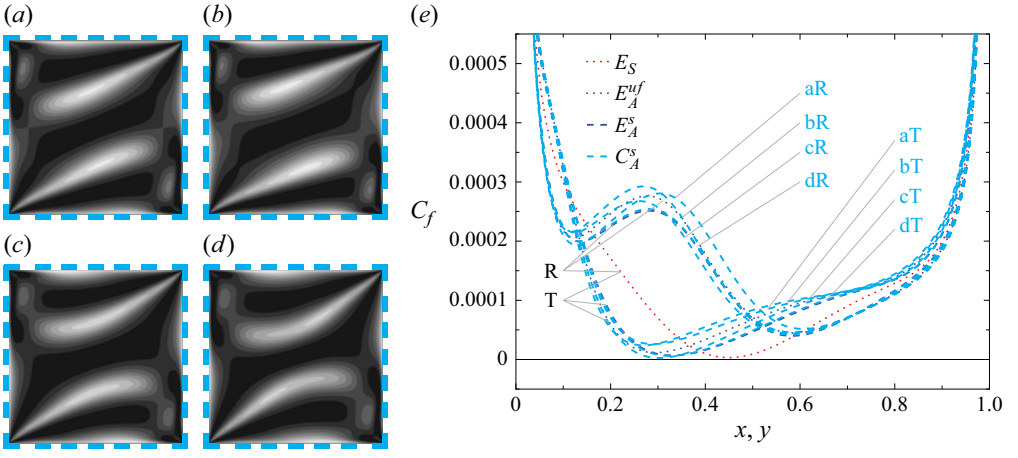


Figure 25. Non-mirror symmetric periodic orbit C_A^s at $Re = 744$. Kinetic energy κ snapshots at (*a*) t_0, (*b*) t_1, (*c*) t_2 and (*d*) t_3 (same instants as for figure 9). (*e*) Friction coefficient C_f along the top (T) and right (R) walls at the same time instants as the snapshots (see labels).

bubble arises. For the rest of the period, C_A^n exhibits somewhat higher friction over most of both walls, roughly averaging to that of E_A^{uf}.

The nodal C_A^n cycle coexisted at $Re = 744$ with a saddle version C_A^s of itself. Four snapshots of C_A^s depicting the κ field are shown in figure 25(*a–d*) at the same instants of those in figure 9(*a–d*). The two solutions, C_A^n and C_A^s, are very close in phase space due to the proximity of FC_A and, since the snapshots have been chosen at analogous phases along a period, they are barely distinguishable. The same goes for $C_f^{T,B}$, for which the only noticeable difference is that the distributions at t_2 (labelled as dT, dR), are closer to those of E_A^s for C_A^s than for C_A^n, on account of the closer immediacy of Hom_A. The same proposition about C_A^n appearing as a short version of $C_{S'}$ where the jets fail to cross the tilt angle limit set by E_A^s and bounce back instead of continuing towards the diagonal and then crossing it, can be extended to C_A^s. It is indeed truer for C_A^s, since the jet angle approaches

https://doi.org/10.1017/jfm.2026.11516 Published online by Cambridge University Press

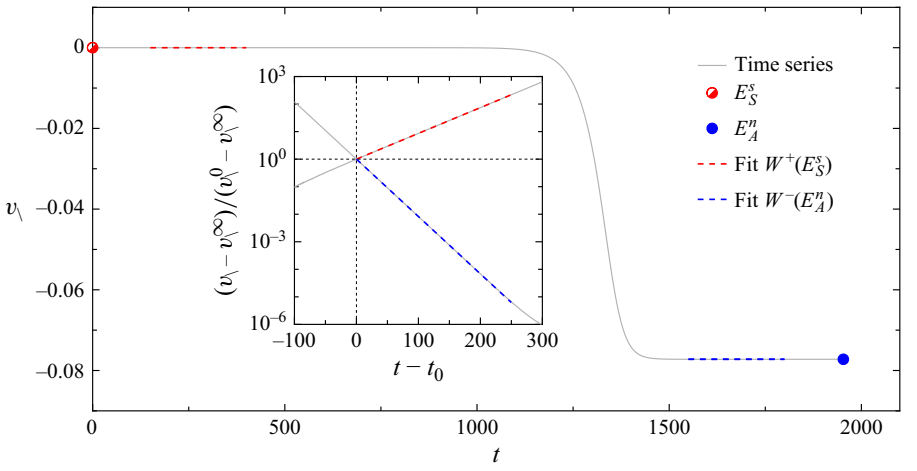


Figure 26. Estimation of the leading eigenvalue of saddle/node equilibrium solutions. A $v_\backslash$ time series (grey line) starting from the vicinity of E_S^s (half-filled red circle) and converging on E_A^n (blue circle) at $Re = 138$ is used to illustrate the method. Exponential fits to the linear regime of departure along the unstable manifold of E_S^s ($W^+(E_S^s)$, dashed red line) and of approach along the stable manifold of E_A^n ($W^-(E_A^n)$, dashed blue) are shown in logarithmic scale in the inset.

that of E_A^s at closer quarters. As a matter of fact, $C_{S'}$ can be viewed, to some extent, as the splicing of C_S with C_A^s and its symmetric at the time instants at which these solutions most resemble E_A^s.

Appendix B. Stability analysis of equilibria and limit cycles

In this appendix, we present the time-stepping-based stability analysis methodology we have employed throughout to estimate the leading eigenvalue of equilibria and the dominant multiplier of limit cycles. The approach is different for equilibria with a single real leading eigenvalue (saddle or node) for equilibria with a complex pair of leading eigenvalues (focus) and for periodic orbits (saddle or node).

When dealing with equilibria with a real leading eigenvalue of multiplicity one, the approach is rather simple. Figure 26 illustrates the procedure for a saddle (E_S^s) and for a node (E_A^n) at $Re = 138$ (see figure 11*a*). In this case, the leading eigenvalue of both can be estimated from the same trajectory, which closely approximates the manifold connecting E_S^s with E_A^n. The E_S^s solution was converged by imposing all symmetries and then the trajectory was computed in full space, with no symmetry restriction. To estimate the leading eigenvalue of a saddle equilibrium, a suitable portion ($t \in [t_0, t_0 + \Delta t]$) of its unstable manifold (W^+) must be isolated within the unimodal linear regime. To guarantee that the analysis is carried out in the linear regime, $t_0 + \Delta t$ must be chosen such that the growing perturbation is still small for nonlinear effects to remain negligible. Unimodality further requires that initial transients be discarded by choosing t_0 sufficiently large for the leading eigenmode to have taken the lead over the rest of the spectrum. In the unimodal linear regime, all flow field variables depart exponentially at the same rate from their value for the steady state, so an exponential fit to $v_\backslash(t)$ following

$$v_\backslash^{fit} = v_\backslash^\infty + \left(v_\backslash^0 - v_\backslash^\infty\right) e^{\lambda(t-t_0)}, \tag{B1}$$

provides the leading eignevalue λ, whcih is positive for a saddle. Of the other two fitting parameters, $v_\backslash^\infty$ returns the value of $v_\backslash$ for the equilibrium whose stability is being

https://doi.org/10.1017/jfm.2026.11516 Published online by Cambridge University Press

assessed, while $v_\backslash^0$ simply corrects for origin effects and is, therefore, inconsequential. The interval $t \in [150, 400]$ of $v_\backslash(t)$ in figure 26 (grey line) has been fitted with (B1) (dashed red) to assess the leading eigenvalue of E_S^s. The inset presents the same data in logarithmic scale, confirming flawless unimodal linearity of the raw data and excellent agreement between data and fit. The slope of the fit is the eigenvalue, in this case, $\lambda = 0.02153868 \pm 3 \times 10^{-8}$.

For a nodal equilibrium, the unimodal linear regime must be sought on its stable manifold (W^-), so any time-stepping trajectory converging the state to a sufficient degree and coming from sufficiently afar can be used. Now, t_0 must be chosen such that the decaying perturbation is small enough for nonlinear effects to have already vanished, while $t_0 + \Delta t$ must be kept clear of the time when the convergence of the solution is nearing machine precision. The same fit (B1) works for a nodal equilibrium, only it will yield negative λ. To assess the leading eigenvalue of E_A^n, we have used the interval $t \in [1550, 1800]$ of $v_\backslash(t)$ and the fit (dashed blue line) produces $\lambda = -0.048030 \pm 2 \times 10^{-6}$.

A similar approach can be used for equilibria featuring a complex leading eigenpair (focus, either stable or unstable). The unimodal linear regime must be chosen analogously, but the fit must take into account the oscillatory departure/approach from/to the steady state. The time series must be fitted with

$$v_\backslash^{fit} = v_\backslash^\infty + \left(v_\backslash^0 - v_\backslash^\infty\right) e^{\lambda_r (t-t_0)} \cos\left(\lambda_i (t - t_0) + \psi_0\right), \tag{B2}$$

where $\lambda = \lambda_r \pm \mathrm{i}\lambda_i$ is the complex pair of eigenvalues and ψ_0 and $v_\backslash^0$ are additional (inconsequential) fitting parameters adjusting the initial phase and amplitude of the oscillation. Alternatively, the analysis can also be done with the assistance of a Poincaré section, interpreting the focus as a limit cycle of zero amplitude and, therefore, unifying the stability analysis framework for foci and limit cycles.

We will illustrate the method on the unstable focus E_S^{uf} and the stable limit cycle C_S^n at $Re = 470$ (see figure 12*a*) from a single run connecting both solutions, and shown in figure 27. Here, E_S^{uf} was computed by imposing all the symmetries of the problem before running the trajectory, this time enforcing the R_π invariance to stabilise C_S^n. The resulting $v_\backslash$ time-series and $(u_\backslash, v_\backslash)$ phase map projection are shown in figures 27(*a*) and 27(*b*) (grey lines), respectively. The trajectory starts from E_S^{uf} (red circle) and ends on C_S^n (pink line, encompassing the last full period). In the time series representation of figure 27(*a*), the trajectory oscillates around E_S^{uf} with increasing amplitude (see a closeup in figure 27*d*) and, after a period of accelerated growth, the amplitude starts to saturate until finally settling at a finite value, that of C_S^n. In the phase map representation of figure 27(*b*), the trajectoy spirals away from E_S^{uf} (see figure 27*e* for an enlarged view around E_S^{uf}, confirming its nature as an unstable focus) before eventually converging onto the closed loop delineated by C_S^n. A fit of the form (B2) to the $v_\backslash(t)$ time series, duly clipped from the linear regime of the unstable manifold $W^+(E_S^{uf})$ ($t \in [60, 250]$), agrees exceptionally well with the raw data (dashed red line in figures 27*d* and 27*e*) and yields a leading eigenvalue for E_S^{uf} of $\lambda = \lambda_r + \mathrm{i}\lambda_i = 0.026857926469 \pm 0.527908203393\mathrm{i}$ with an estimated error of $\pm 2 \times 10^{-12}$ in both the real and imaginary parts.

To assess the leading multiplier of a periodic orbit (or a focus equilibrium) without having to resort to Floquet theory, it is convenient to deploy a Poincaré section $\mathcal{S}$ and examine the resulting discrete-time dynamical system (An *et al.* 2019; Wang *et al.* 2025). The Poincaré (or first return) map is

https://doi.org/10.1017/jfm.2026.11516 Published online by Cambridge University Press

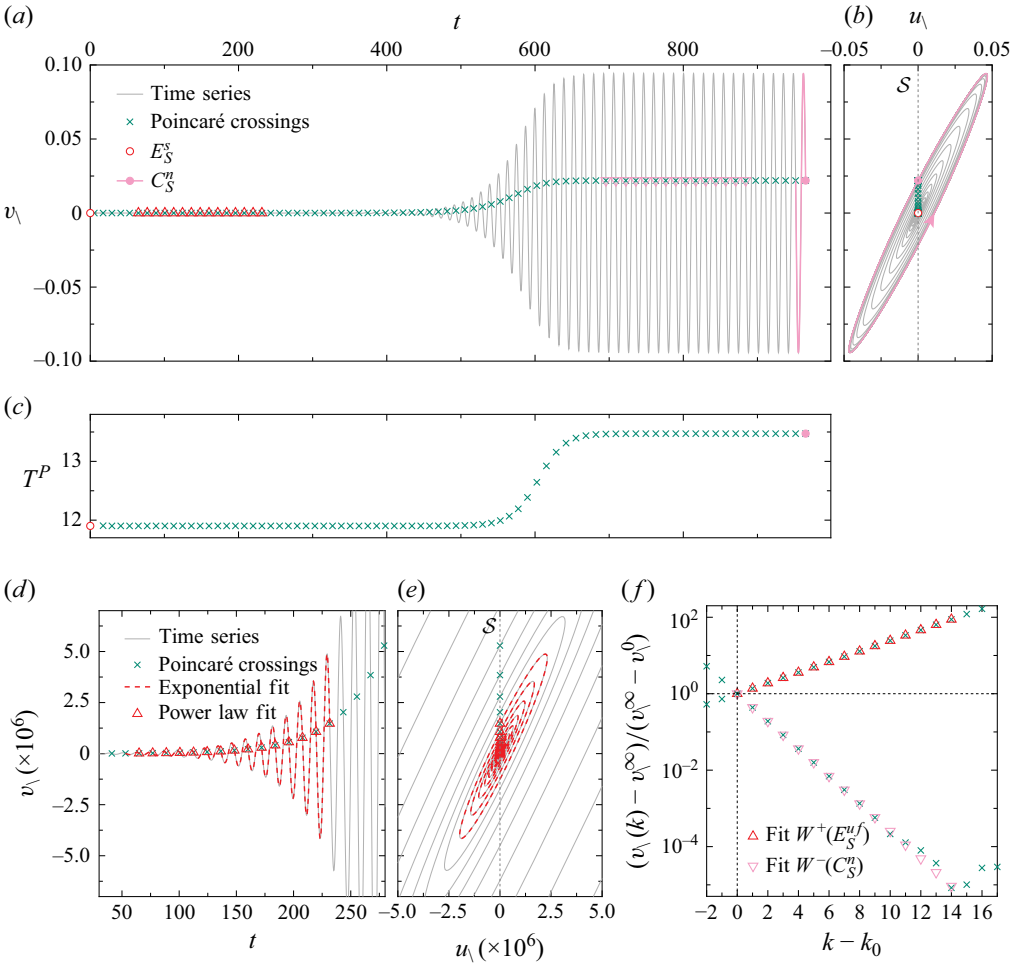


Figure 27. Estimation of the leading eigenvalue of foci and the dominant multiplier of limit cycles. (*a*) $v_\backslash$ time series (grey line) and (*b*) $(u_\backslash, v_\backslash)$ phase map projection starting from the vicinity of E_S^{uf} (red circle) and converging on C_S^n (pink line) at $Re = 470$. Also shown are crossings of the Poincaré section $\mathcal{S}$ (green crosses). (*c*) Sequence of flight times T^P between consecutive Poincaré crossings. Close-ups of (*d*) $v_\backslash(t)$ and (*e*) $(u_\backslash, v_\backslash)$, on the linear regime of the unstable manifold of E_S^{uf} (W^+). Superposed are the exponential fit (red dashed line) to the time series $v_\backslash(t)$ and the power law fit (red triangles) to the corresponding Poincaré crossings $v_\backslash(k)$. (*f*) Power law fits to Poincaré crossings in the linear regime of $W^+(E_S^{uf})$ (red triangles) and of $W^-(C_S^n)$ (the stable manifold of C_S^n, pink triangles), shown in logarithmic scale.

$$\begin{array}{rccc} \mathcal{P}: & \mathcal{S} & \longrightarrow & \mathcal{S} \\ & \boldsymbol{a}^P & \longmapsto & \mathcal{P}\left(\boldsymbol{a}^P\right) = \phi_{T^P}\left(\boldsymbol{a}^P\right) \end{array} \tag{B3}$$

where $\boldsymbol{a} = (\boldsymbol{u}, p)$ defines the state of the continuous-time dynamical system (the 4LDSSC flow problem), $\phi_\tau(\boldsymbol{a})$ is the flow generated by evolving state $\boldsymbol{a}$ for a lapse τ and $\boldsymbol{a}^P$ is a state on $\mathcal{S}$. Repeated application of the map generates a sequence $\boldsymbol{a}^P(k)$ with associated crossing times $t^P(k)$, which are in fact obtained as a post-process of the continuous-time dynamical system evolution by second-order interpolation of $\mathcal{S}$-intersections. The sequence of flight lapses between consecutive crossings is then obtained as $T^P(k) = t^P(k) - t^P(k-1)$. Here, we have used the $u_\backslash$ time series to define the Poincaré section

https://doi.org/10.1017/jfm.2026.11516 Published online by Cambridge University Press

as $\mathcal{S} = \{\boldsymbol{a} : u_\backslash = u_\backslash^P,\ \partial_t u_\backslash < 0\}$, where the value $u_\backslash^P$ must always be chosen such that the portion of the trajectory employed in the stability analysis intersects $\mathcal{S}$ once every oscillation. As evident from figures 27(*a*) and 27(*b*), $u_\backslash^P = 0$ works for the stability analysis of solutions possessing either the $M_\backslash$ or the ST symmetries, so it is a suitable choice for both E_S^{uf} (or E_S^f whenever stable) and C_S (and also $C_{S'}$). Different (finite) values were required in the analysis of E_A^f or C_A. In general, a reasonable choice for periodic orbits is the average value of $u_\backslash$ over a full period, while for foci, it is mandatory to use the value of $u_\backslash$ for the solution if the trajectory is to intersect $\mathcal{S}$ from early on during the linear regime. The state of the system on $\mathcal{S}$ at crossings k is obtained from the time series as $\boldsymbol{a}^P(k) = \boldsymbol{a}(t^P(k))$ and, in particular, $v_\backslash^P(k) = v_\backslash(t^P(k))$ is shown as a function of $t^P(k)$ in figures 27(*a*) and 27(*d*), and of $u_\backslash^P(k) = u_\backslash^P = 0$ in figures 27(*b*) and 27(*e*) (green crosses). The sequence of flight times T^P between consecutive $\mathcal{S}$ crossings is shown in figure 27(*c*). Its value close to the cycle is fairly constant and provides an accurate estimate of the period. Accordingly, it can be computed by averaging the first crossings away from the solution if unstable (discarding initial transients) or the last approaching it if stable. Thus computed, the periods of E_S^{uf} (interpreted as a limit cycle) and C_S^n are $T_{E_S^{uf}} = 11.902041420 \pm 9 \times 10^{-8}$ and $T_{C_S^n} = 13.472369 \pm 3 \times 10^{-6}$, respectively. To analyse the stability, an interval $k \in [k_0, k_0 + \Delta k]$ must be extracted from the $v_\backslash^P(k)$ sequence following the same criteria that were used when cropping $v_\backslash(t)$ for the analysis of equilibria. In the linear regime, a power law fit to the sequence $v_\backslash^P(k)$ of Poincaré crossings following

$$v_\backslash^{fit} = v_\backslash^\infty + \left(v_\backslash^0 - v_\backslash^\infty\right)\mu^{k-k_0}, \tag{B4}$$

yields the multiplier μ (<1 for a stable limit cycle, >1 for unstable). In this case, $v_\backslash^\infty$ is the estimated value of $v_\backslash$ at the intersection of the limit cycle with $\mathcal{S}$, while $v_\backslash^0$ is again an irrelevant fitting parameter accounting for discrete-time origin effects. The subsequence of $\mathcal{S}$ crossings chosen for the analysis of C_S^n is $k \in [57, 72]$, corresponding to $t \in [690, 900]$ of the continuous-time system. The fit is shown in figure 27(*a*) and, in logarithmic scale, in figure 27(*f*) (pink triangles). Although the fit is compellingly convincing over most of the subsequence, the loss of linear unimodality is apparent at the tail as convergence of the periodic orbit is already reaching machine epsilon. The slope in figure 27(*f*) is the natural logarithm of the multiplier, which for C_S^n gives an estimate $\mu = 0.43696 \pm 2 \times 10^{-5}$. The subsequence employed in the analysis of E_S^{uf} as a limit cycle of zero amplitude is $k \in [5, 20]$, corresponding to $t \in [60, 250]$. The power law fit, presented in figures 27(*a*) and 27(*d*) (red triangles), is indistinguishable from the raw data. The slope in the logarithmic representation of figure 27(*f*) yields $\mu = 1.376665337 \pm 2 \times 10^{-9}$ for E_S^{uf}. The period and dominant multiplier of a focus equilibrium can be readily converted into the dominant complex pair of eigenvalues following

$$\lambda_r = \frac{1}{T}\log\mu, \quad \lambda_i = \frac{2\pi}{T}. \tag{B5}$$

For E_S^{uf}, we obtain $\lambda = 0.0268579264 \pm 0.527908203\mathrm{i}$, with an estimated error of $3 \times 10^{-10} \pm 4 \times 10^{-9}\mathrm{i}$, an exceptionally good match with the previous determination using (B2).

https://doi.org/10.1017/jfm.2026.11516 Published online by Cambridge University Press

References

Abouhamza, A. & Pierre, R. 2003 A neutral stability curve for incompressible flows in a rectangular driven cavity. *Math. Comput. Model.* **38** (1–2), 141–157.

Aidun, C.K., Triantafillopoulos, N.G. & Benson, J.D. 1991 Global stability of a lid-driven cavity with throughflow – flow visualization studies. *Phys. Fluids A* **3** (9), 2081–2091.

Albensoeder, S., Kuhlmann, H.C. & Rath, H.J. 2001 Three-dimensional centrifugal-flow instabilities in the lid-driven-cavity problem. *Phys. Fluids* **13** (1), 121–135.

An, B., Bergada, J.M. & Mellibovsky, F. 2019 The lid-driven right-angled isosceles triangular cavity flow. *J. Fluid Mech.* **875**, 476–519.

An, B., Bergada, J.M., Mellibovsky, F. & Sang, W.M. 2020*a* New applications of numerical simulation based on lattice boltzmann method at high reynolds numbers. *Comput. Math. Appl.* **79** (6), 1718–1741.

An, B., Bergada, J.M., Mellibovsky, F., Sang, W.M. & Xi, C. 2020*b* Numerical investigation on the flow around a square cylinder with an upstream splitter plate at low Reynolds numbers. *Meccanica* **55** (5), 1037–1059.

An, B., Bergada, J.M., Sang, W., Li, D. & Mellibovsky, F. 2023 Square cavity flow driven by two mutually facing sliding walls. *J. Zhejiang Univ. Sci.* **24** (7), 612–624.

An, B., Mellibovsky, F., Bergada, J.M. & Sang, W.M. 2020*c* Towards a better understanding of wall-driven square cavity flows using the lattice Boltzmann method. *Appl. Math. Model.* **82**, 469–486.

Andereck, C.D., Liu, S.S. & Swinney, H.L. 1986 Flow regimes in a circular Couette system with independently rotating cylinders. *J. Fluid Mech.* **164**, 155–183.

Auteri, F., Parolini, N. & Quartapelle, L. 2002*a* Numerical investigation on the stability of singular driven cavity flow. *J. Comput. Phys.* **183** (1), 1–25.

Auteri, F., Quartapelle, L. & Vigevano, L. 2002*b* Accurate omega-psi spectral solution of the singular driven cavity problem. *J. Comput. Phys.* **180** (2), 597–615.

Batoul, A., Khallouf, H. & Labrosse, G. 1994 A direct spectral solver of the 2d/3d unsteady Stokes problem – application to the 2d square driven cavity. *C. R. Acad. Sci. II.* **319** (12, 1), 1455–1461.

Benson, J.D. & Aidun, C.K. 1992 Transition to unsteady nonperiodic state in a through-flow lid-driven cavity. *Phys. Fluids A* **4** (10), 2316–2319.

Boffetta, G. & Ecke, R.E. 2012 Two-dimensional turbulence. *Annu. Rev. Fluid Mech.* **44**, 427–451.

Boppana, V.B.L. & Gajjar, J.S.B. 2010 Global flow instability in a lid-driven cavity. *Intl J. Num. Meth. Fluids* **62** (8), 827–853.

Botella, O. 1997 On the solution of the Navier–Stokes equations using Chebyshev projection schemes with third-order accuracy in time. *Comput. Fluids* **26** (2), 107–116.

Botella, O. & Peyret, R. 1998 Benchmark spectral results on the lid-driven cavity flow. *Comput. Fluids* **27** (4), 421–433.

Botella, O. & Peyret, R. 2001 Computing singular solutions of the Navier–Stokes equations with the Chebyshev-collocation method. *Intl J. Num. Methods Fluids* **36** (2), 125–163.

Bruneau, C.H. & Saad, M. 2006 The 2d lid-driven cavity problem revisited. *Comput. Fluids* **35** (3), 326–348.

Cadou, J.M., Guevel, Y. & Girault, G. 2012 Numerical tools for the stability analysis of 2d flows: application to the two- and four-sided lid-driven cavity. *Fluid Dyn. Res.* **44**, 031403.

Cazemier, W., Verstappen, R.W.C.P. & Veldman, A.E.P. 1998 Proper orthogonal decomposition and low-dimensional models for driven cavity flows. *Phys. Fluids* **10** (7), 1685–1699.

Chen, S. & Doolen, G.D. 1998 Lattice Boltzmann method for fluid flows. *Annu. Rev. Fluid Mech.* **30**, 329–364.

Chen, K.-T., Tsai, C.-C. & Luo, W.-J. 2013 Multiplicity flow solutions in a four-sided lid-driven cavity. In *Frontiers of Green Building, Materials and Civil Engineering III, PTS. 1–3* (ed. J.C.M. Kao, W.P. Sung & R. Chen), Applied Mechanics and Materials, vol. 368–370, p. 838+. Natl Chin Yi Univ Technol, Natl Cheng Kung Univ; Natl Sun Yan Sen Univ; Natl Chi Nun Univ; ChienKuo Technol Univ; Control Engn & Informat Sci Res Assoc; Int Frontiers Sci & Technol Res Assoc; Trans Tech Publicat, 3rd International Conference on Green Building, Materials and Civil Engineering (GBMCE 2013), Taiwan, PEOPLES R CHINA, AUG 21–23, 2013.

Coles, D. 1965 Transition in circular Couette flow. *J. Fluid Mech.* **21**, 385–425.

Dangelmayr, G., Armbruster, D. & Neveling, M. 1985 A codimension 3 bifurcation for the laser with saturable absorber. *Z. Phys. B Condens. Matter.* **59** (3), 365–370.

Dangelmayr, G., Neveling, M. & Armbruster, D. 1986 Structurally stable phase portraits for the 5-dimensional Lorenz equations. *Z. Phys. B Condens. Matter.* **64** (4), 491–501.

Fortin, A., Jardak, M., Gervais, J.J. & Pierre, R. 1997 Localization of Hopf bifurcations in fluid flow problems. *Intl J. Numer. Meth. Fluids* **24** (11), 1185–1210.

https://doi.org/10.1017/jfm.2026.11516 Published online by Cambridge University Press

GASPARD, P. 1990 Measurement of the instability rate of a far-from-equilibrium steady-state at an infinite period bifurcation. *J. Phys. Chem.* **94** (1), 1–3.

GHIA, U., GHIA, K.N. & SHIN, C.T. 1982 High-re solutions for incompressible-flow using the Navier–Stokes equations and a multigrid method. *J. Comput. Phys.* **48** (3), 387–411.

GRESHO, P.M. & CHAN, S.T. 1990 On the theory of semiimplicit projection methods for viscous incompressible-flow and its implementation via a finite-element method that also introduces a nearly consistent mass matrix.2. implementation. *Intl J. Numer. Meth. Fluids* **11** (5), 621–659.

GUPTA, M.M. & KALITA, J.C. 2005 A new paradigm for solving Navier–Stokes equations: streamfunction-velocity formulation. *J. Comput. Phys.* **207** (1), 52–68.

GUPTA, M.M., MANOHAR, R.P. & NOBLE, B. 1981 Nature of viscous flows near sharp corners. *Comput. Fluids* **9** (4), 379–388.

HOF, B., VAN DOORNE, C.W.H., WESTERWEEL, J., NIEUWSTADT, F.T.M., FAISST, H., ECKHARDT, B., WEDIN, H., KERSWELL, R.R. & WALEFFE, F. 2004 Experimental observation of nonlinear traveling waves in turbulent pipe flow. *Science* **305** (5690), 1594–1598.

HOU, S.L., ZOU, Q., CHEN, S.Y., DOOLEN, G. & COGLEY, A.C. 1995 Simulation of cavity flow by the lattice Boltzmann method. *J. Comput. Phys.* **118** (2), 329–347.

ITANO, T. & TOH, S. 2001 The dynamics of bursting process in wall turbulence. *J. Phys. Soc. Japan* **70** (3), 703–716.

JIMENEZ, J. 1990 Transition to turbulence in 2-dimensional Poiseuille flow. *J. Fluid Mech.* **218**, 265–297.

KALITA, J.C. & GOGOI, B.B. 2016 A biharmonic approach for the global stability analysis of 2d incompressible viscous flows. *Appl. Math. Model.* **40** (15–16), 6831–6849.

KHORASANIZADE, S. & SOUSA, J.M.M. 2014 A detailed study of lid-driven cavity flow at moderate Reynolds numbers using Incompressible SPH. *Intl J. Numer. Meth. Fluids* **76** (10), 653–668.

KNOBLOCH, E. 1986 Normal forms for bifurcations at a double zero eigenvalue. *Phys. Lett. A* **115** (5), 199–201.

KOSEFF, J.R. & STREET, R.L. 1984 The lid-driven cavity flow - a synthesis of qualitative and quantitative observations. *ASME J. Fluid Engng* **106** (4), 390–398.

KUHLMANN, H.C. & ROMANÒ, F. 2019 The lid-driven cavity. In *Computational Modelling of Bifurcations and Instabilities in Fluid Dynamics* (ed. A. Gelfgat), vol. 8, pp. 233–309. Springer International Publishing.

KUZNETSOV, Y.A. 2023 *Elements of Applied Bifurcation Theory*, 4th edn. Springer.

LI, C.G. & MAA, J.P.-Y. 2017 Lattice Boltzmann simulations of three-dimensional incompressible flows in a four-sided lid driven cavity. *Fluid Dyn. Res.* **49** (2), 025507.

DE LOZAR, A., MELLIBOVSKY, F., AVILA, M. & HOF, B. 2012 Edge state in pipe flow experiments. *Phys. Rev. Lett.* **108** (21), 214502.

MARCHI, C.H., SUERO, R. & ARAKI, L.K. 2009 The lid-driven square cavity flow: numerical solution with a 1024×1024 grid. *J. Braz. Soc. Mech. Sci. Engng* **31** (3), 186–198.

MELLIBOVSKY, F. & MESEGUER, A. 2015 A mechanism for streamwise localisation of nonlinear waves in shear flows. *J. Fluid Mech.* **779**, R1.

MESEGUER, A., ALONSO, A., BATISTE, O., AN, B. & MELLIBOVSKY, F. 2024 Bifurcation analysis in the regularized four-sided cavity flow: equilibrium states in a D_2-symmetric fluid system. *Phys. Fluids* **36** (6), 064104.

MESEGUER, A., MELLIBOVSKY, F., AVILA, M. & MARQUES, F. 2009 Families of subcritical spirals in highly counter-rotating Taylor–couette flow. *Phys. Rev. E* **79**, 036309.

MOLENAAR, D., CLERCX, H.J.H. & VAN HEIJST, G.J.F. 2005 Transition to chaos in a confined two-dimensional fluid flow. *Phys. Rev. Lett.* **95** (10), 104503.

MURDOCK, J.R., ICKES, J.C. & YANG, S.L. 2017 Transition flow with an incompressible lattice Boltzmann method. *Adv. Appl. Math. Mech.* **9** (5), 1271–1288.

NEWHOUSE, S., RUELLE, D. & TAKENS, F. 1978 Occurrence of strange axiom a attractors near quasi periodic flows on tm, m is greater than or equal to 3. *Commun. Math. Phys.* **64** (1), 35–40.

NON, E., PIERRE, R. & GERVAIS, J.J.2006 Linear stability of the three-dimensional lid-driven cavity. *Phys. Fluids* **18** (8), 084103.

NURIEV, A.N., EGOROV, A.G. & ZAITSEVA, O.N. 2016 Bifurcation analysis of steady-state flows in the lid-driven cavity. *Fluid Dynam. Res.* **48** (6), 061405. 6th International Symposium on Instability and Bifurcations in Fluid Dynamics (BIFD), ESPCI, Paris, FRANCE, JUL 15-17, 2015.

PENG, Y.F., SHIAU, Y.H. & HWANG, R.R. 2003 Transition in a 2-d lid-driven cavity flow. *Comput. Fluids* **32** (3), 337–352.

PERUMAL, D.A. & DASS, A.K. 2011 Multiplicity of steady solutions in two-dimensional lid-driven cavity flows by lattice Boltzmann method. *Comput. Math. Appl.* **61** (12), 3711–3721. 6th International Conference for Mesoscopic Methods in Engineering Science (ICMMES-09), S China Univ Technol (SCUT), Guangzhou, PEOPLES R CHINA, JUL 13–17, 2009.

https://doi.org/10.1017/jfm.2026.11516 Published online by Cambridge University Press

POLIASHENKO, M. & AIDUN, C.K. 1995 A direct method for computation of simple bifurcations. *J. Comput. Phys.* **121** (2), 246–260.

PROCACCIA, I. 1988 Universal properties of dynamically complex-systems – the organization of chaos. *NATURE* **333** (6174), 618–623.

QIAN, Y.H., D'HUMIÈRES, D. & LALLEMAND, P. 1992 Lattice BGK models for Navier–Stokes equation. *Europhys. Lett.* **17** (6BIS), 479–484.

RITTER, P., MELLIBOVSKY, F. & AVILA, M. 2016 Emergence of spatio-temporal dynamics from exact coherent solutions in pipe flow 18, 083031.

ROMANÒ, F. & KUHLMANN, H.C. 2017 Smoothed-profile method for momentum and heat transfer in particulate flows. *Intl J. Num. Methods Fluids* **83** (6), 485–512.

RUELLE, D. & TAKENS, F. 1971 On the nature of turbulence. *Commun. Math. Phys.* **20** (3), 167–192.

SAHIN, M. & OWENS, R.G. 2003*a* A novel fully implicit finite volume method applied to the lid-driven cavity problem – part I: high Reynolds number flow calculations. *Intl J. Numer. Meth. Fluids* **42** (1), 57–77.

SAHIN, M. & OWENS, R.G. 2003*b* A novel fully-implicit finite volume method applied to the lid-driven cavity problem. Part ii. Linear stability analysis. *Intl J. Numer. Meth. Fluids* **42** (1), 79–88.

SCHREIBER, R. & KELLER, H.B. 1983 Driven cavity flows by efficient numerical techniques. *J. Comput. Phys.* **49** (2), 310–333.

SHANKAR, P.N. & DESHPANDE, M.D. 2000 Fluid mechanics in the driven cavity. *Annu. Rev. Fluid Mech.* **32**, 93–136.

SHEN, J. 1991 Hopf-bifurcation of the unsteady regularized driven cavity flow. *J. Comput. Phys.* **95** (1), 228–245.

SMITH, J.A. & LARGIER, J.L. 1995 Observations of nearshore circulation – rip currents. *J. Geophys. Res.-Oceans* **100** (C6), 10967–10975.

TAKENS, F. 1974 Forced oscillations and bifurcations. *Commun. Math. Inst.* **2**, 1–111.

THEOFILIS, V., DUCK, P.W. & OWEN, J. 2004 Viscous linear stability analysis of rectangular duct and cavity flows. *J. Fluid Mech.* **505**, 249–286.

TIESINGA, G., WUBS, F.W. & VELDMAN, A.E.P. 2002 Bifurcation analysis of incompressible flow in a driven cavity by the Newton–Picard method. *J. Comput. Appl. Math.* **140** (1–2, SI), 751–772. 9th International Congress on Computational and Applied Mathematics, Univ Leuven, Leuven, Belgium, Jul 17-21, 2000.

VANKA, S.P. 1986 Block-implicit multigrid solution of Navier–Stokes equations in primitive variables. *J. Comput. Phys.* **65** (1), 138–158.

WAHBA, E.M. 2009 Multiplicity of states for two-sided and four-sided lid driven cavity flows. *Comput. Fluids* **38** (2), 247–253.

WAHBA, E.M. 2011 Numerical simulations of flow bifurcations inside a driven cavity. *CFD Lett.* **3** (2), 100–110.

WANG, B., AYATS, R., DEGUCHI, K., MESEGUER, A. & MELLIBOVSKY, F. 2025 Feigenbaum universality in subcritical Taylor–Couette flow. *J. Fluid Mech.* **1010**, A36.

WANG, B., MELLIBOVSKY, F., AYATS, R., DEGUCHI, K. & MESEGUER, A. 2023 Mean structure of the supercritical turbulent spiral in Taylor–Couette flow. *Phil. Trans. R. Soc. Lond. A* **381** (2246), 20220112.

WELLS, M.G. & VAN HEIJST, G.J.F. 2003 A model of tidal flushing of an estuary by dipole formation. *Dyn. Atmos. Oceans* **37** (3), 223–244.

ZHUO, C., ZHONG, C., GUO, X. & CAO, J. 2013 MRT-LBM simulation of four-lid-driven cavity flow bifurcation. *Procedia Engng* **61**, 100–107.

ZHUO, C., ZHONG, C., GUO, X. & CAO, J. 2015 Numerical investigation of four-lid-driven cavity flow bifurcation using the multiple-relaxation-time lattice Boltzmann method. *Comput. Fluids* **110** (SI), 136–151.

https://doi.org/10.1017/jfm.2026.11516 Published online by Cambridge University Press